RESEARCH ARTICLE

ADVANCED FUNCTIONAL MATERIALS
www.afm-journal.de

High-Performance Low-Emissivity Paints Enabled by N-Doped Poly(benzodifurandione) (n-PBDF) for Energy-Efficient Buildings

Xiaojie Liu, Won-June Lee, Daniel William Carne, Yanpei Tian, Andrea Felicelli, Yue Lei, Joseph A. Romo, Liyan You, Zixin Xiong, Orlando Gabriel Rivera Gonzalez, Abdulrahman Aljwirah, Qiaoqiang Gan, Jianguo Mei, and Xiulin Ruan**

Low-emissivity (low-e) paints reduce radiative heat exchange between buildings and the environment, stabilizing indoor climates and lowering air conditioning demand. However, low-cost, durable, and colored low-e paints have yet to be demonstrated. Here, an approach is proposed using n-doped poly(benzodifurandione) (n-PBDF), a transparent organic conducting polymer, coated over colored commercial paints. This achieves a low thermal emissivity of 0.19 in the mid-infrared spectrum, attributed to the efficient charge transport of delocalized π-electrons in n-PBDF structure. The reduction in thermal emissivity aids in regulating building temperatures by minimizing heat transfer between buildings and their surroundings across diverse climate zones and seasons. The n-PBDF coating preserves the underlying paint's color due to its high visible transparency, meeting aesthetic requirements. It also shows strong stability in accelerated indoor weathering tests, ensuring long-term performance. Simulations estimate annual HVAC energy savings of over 10,800 kWh in San Francisco and 5,500 kWh in Chicago for the typical mid-rise apartments. The paint's versatility, scalability, and durability make it suitable for buildings, vehicles, and greenhouses, aiding urban heat island mitigation.

1. Introduction

Throughout history, humans have sought to create thermally comfortable architecture. Today, energy demand in the building sector is surging due to population growth and urbanization, exacerbated by climate fluctuations such as extreme heat and cold, which increase energy loads on buildings. Buildings account for approximately 40% of global energy consumption and 33% of carbon emissions.[1] Notably, over 40% of building energy is used for heating, ventilation, and air conditioning (HVAC) systems to maintain indoor comfort.[2] Addressing this demand is crucial for meeting the emission reduction targets set by the Paris Agreement.[1]

There are two primary strategies for thermal regulation in buildings: active methods, which rely on energy-intensive air conditioning,[3] and passive methods, which use advanced materials to modulate heat transfer naturally.[4–6] These approaches include thermochromic windows,[7–11] thermal insulation materials,[12,13] and daytime radiative cooling materials.[14–23] Walls account for ≈25% of heat exchange between interior and exterior environments, with exterior surfaces exchanging heat through convection and infrared radiation.[24] Traditional materials like brick, stone, glass, and concrete have high thermal emissivity, causing temperature swings and discomfort.[25] High-emissivity materials can lead to overheating in hot climates and excessive heat loss in cold climates. To address these challenges, radiative cooling materials can be developed to have high emissivity only in the sky window band (8–13 µm), allowing for heat exchange in this band while rejecting heat out of this band from hot surroundings.[26–28] However, this does not solve cold climate issues, where heat loss remains a concern.

On the other hand, low-emissivity (low-e) paints are characterized by their low thermal emissivity across the entire mid-infrared (MIR) band (2.5–20 µm) and often in the near-infrared (NIR) band (0.8–2.5 µm). This property enables them to minimize heat exchange with the surrounding environment, creating a more stable indoor climate in both hot and cold conditions. Most commercial low-e paints use metallic mate-

---

X. Liu, D. W. Carne, A. Felicelli, Z. Xiong, O. G. R. Gonzalez, A. Aljwirah, X. Ruan
School of Mechanical Engineering and Birck Nanotechnology Center
Purdue University
West Lafayette, IN 47907, USA
E-mail: ruan@purdue.edu

X. Liu, W.-J. Lee, J. A. Romo, L. You, J. Mei
James Tarpo Jr. and Margaret Tarpo Department of Chemistry
Purdue University
West Lafayette, IN 47907, USA
E-mail: jgmei@purdue.edu

Y. Tian, Y. Lei, Q. Gan
Material Science Engineering
King Abdullah University of Science and Technology (KAUST)
Thuwal 23955–6900, Saudi Arabia

The ORCID identification number(s) for the author(s) of this article can be found under https://doi.org/10.1002/adfm.202419685

[Correction added on November 22, 2025, after first online publication: A typo error corrected in the affiliation of one of the authors in this version.]

DOI: 10.1002/adfm.202419685

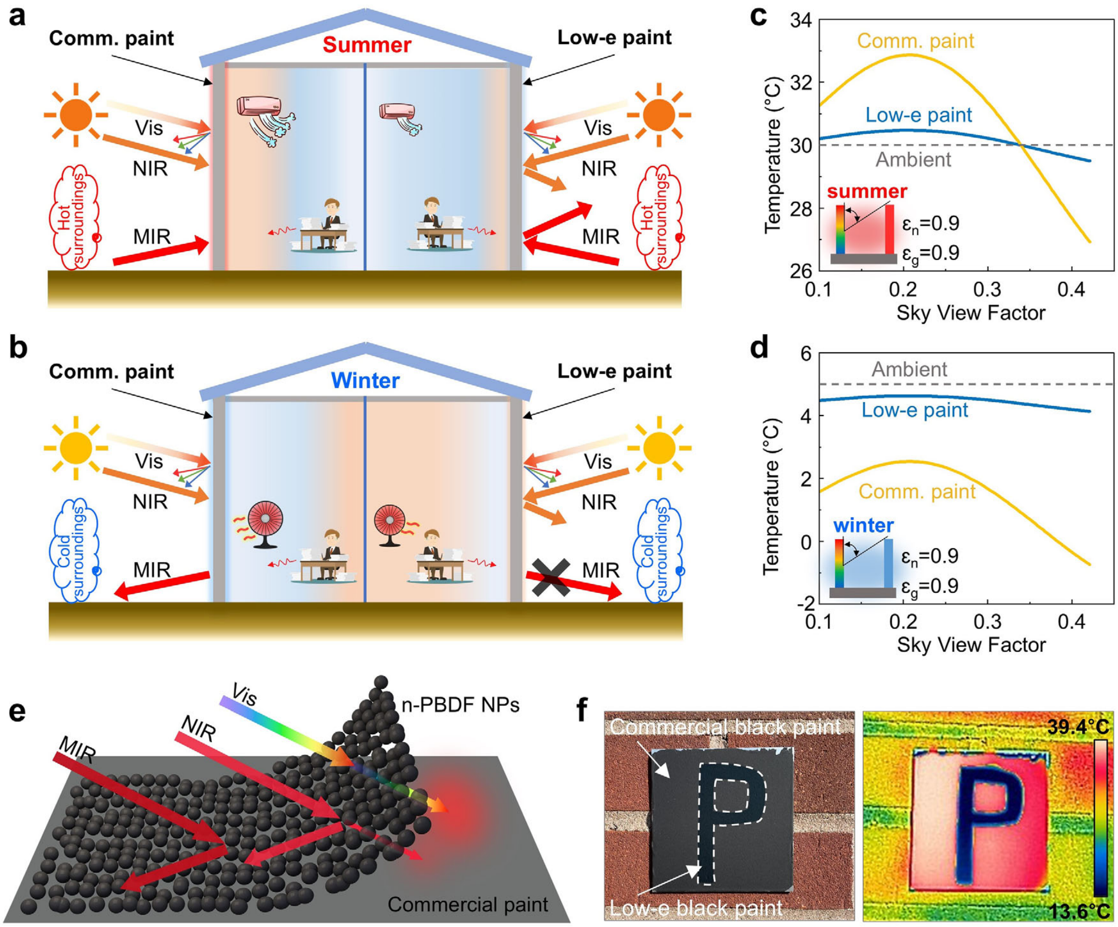

Figure 1. Concept of colored low-e paint for building thermal regulation. Schematics of the heat exchange process between building walls coated with colored low-e paint and the surroundings in a) summer and b) winter. c,d) Surface temperature of walls coated with low-e paint and commercial paint as a function of the sky view factor (SVF) in c) summer and d) winter. e) Schematic illustrating the working principle of the colored low-e paint. The bottom layer is a colored commercial paint that provides the desired appearance to satisfy aesthetic demands. The top layer is the visible-transparent n-PBDF-based coating layer with high thermal reflectance in the infrared region. f) Photograph (left) and corresponding IR image (right) showing a low-e "P" contrasting with the commercial black paint with high thermal emittance.

rials like silver particles or aluminum flakes to achieve low emissivity.[29–34] However, these paints have a metallic appearance that does not meet aesthetic requirements and can lose their low-emissivity performance over time due to the oxidation of metal particles. In contrast, recent research by Peng et al.[31] introduced a bilayer paint with an IR-transparent colored top layer containing inorganic nanoparticles (e.g., Prussian blue, iron oxide, goethite, zinc oxide) and a low-e bottom layer of aluminum flakes dispersed in an IR-transparent organic binder. While promising, the high cost of IR-transparent binders limits scalability. Conducting polymers like PEDOT:PSS[35,36] offer an alternative to metals for low-e paints. However, they face challenges, including the need for external dopants, additional post-treatment and thermal drying processes, a lack of color, stability issues under environmental stress (e.g., moisture and UV exposure), lower conductivity, and thicker films with reduced light transmittance. To date, no studies have yet demonstrated scalable, colored, and durable low-e paints.

To tackle these challenges, we propose an approach using an ultrathin layer of a novel conducting polymer, n-doped poly(benzodifurandione) (n-PBDF), facilely sprayed on top of commercial paints in a scalable and energy-efficient manner. Unlike metals used in commercial low-e paints, here n-PBDF provides intrinsic low-e functionality from its self-doping state across the entire IR range, offering substantial cost-saving potential in both process and material costs.[37] Our design places the low-e layer on top of the colored layer, eliminating the demand for costly IR-transparent binders and low-e metallic/inorganic nanoparticles.[31,38,39] The n-PBDF coating reveals the colors of the underlying layer, maintaining the aesthetic appeal of commercial paints. The n-PBDF coating layer shows strong stability in accelerated indoor weathering tests, ensuring long-term performance. This solution-processed n-PBDF coating can be easily applied and helps reject MIR thermal radiation in hot summers while minimizing heat loss in winter (**Figure** 1a,b). A theoretical model demonstrates that low-e walls maintain temperatures with smaller fluctuations compared to walls with commercial paint (Figure 1c,d). This highlights the potential of our colored low-e paint as an effective energy-saving strategy, reducing HVAC energy consumption by minimizing radiative heat exchange.

2. Results and Discussion

2.1. Material Design

A low-e and colored paint should selectively reflect visible light to meet the aesthetic functionality and strongly reflect infrared radiation to impede heat exchange with the ambient. To date, colored commercial paints have always shown high thermal emissivity because organic binders, one of the essential components, display emissive peaks over IR wavelengths. Here, starting from colored commercial paint as the base layer, a visible-transparent and IR-reflective ultrathin layer is applied at the top, allowing the paint color to be preserved while achieving high IR reflectance. The top layer consisted of n-doped PBDF colloids (n-PBDF), an organic conjugated conductive polymer (Figure 1e). Starting from a wavelength of 0.8 µm, the top coating shows an elevated reflectance and reduces the solar heating gain over the NIR region, facilitating energy saving during the summer. Meanwhile, the top layer shows high reflection over the MIR wavelengths, where the thermal radiation of room-temperature objects is concentrated. This minimizes the thermal radiation exchange between the building envelopes and surroundings and facilitates the thermal regulation of buildings across seasons. The low emissivity of n-PBDF can be visualized using a “P” pattern of n-PBDF sprayed on a printing paper surrounded by commercial black paint (Figure 1f). Despite the same temperature, the dark blue color of the low-e “P” pattern in the IR image clearly demonstrates the low emissivity of the n-PBDF layer, because it emits less thermal radiation to the IR camera.

2.2. Conducting Polymer Ink Coating for Low-E Paints

n-PBDF stands out because of its exceptional electrical conductivity and superior optical transparency in the visible light spectrum, as well as its remarkable stability under air, moisture, and thermal conditions, due to the efficient charge transport of delocalized π-electrons in the rigid, extended π-backbones.[40,41] We have successfully integrated this transparent low-e film with common exterior-colored paints, demonstrating its potential for broad application in enhancing the energy efficiency and optical performance of architectural and vehicular coatings. **Figure 2a** provides a comprehensive schematic illustration of the process involving the coating of commercial paints of various colors, followed by the top coating of the prepared n-PBDF ink solution through a large-scale spray coating process (Note S1, Supporting Information). Notably, the utilization of environmentally friendly alcohol-based solvents facilitates the preservation of the rigid backbone structure of n-PBDF during its formulation into a scalable sprayable ink. The inset shows a photograph of the prepared solution containing more than 300 mL of the n-PBDF ink solution, highlighting the solution properties, excellent dispersity, good stability, and homogenous ink. This indicates the universal potential of n-PBDF ink to retrofit colored surfaces to preserve color while enabling low-e properties regardless of scale, including large building walls or vehicle exteriors.

The scanning electron microscopy (SEM) images in Figure 2b–d depict the surface morphology of the commercial black paint, n-PBDF particles, and a layer of n-PBDF coated on the commercial black paint. The commercial black paint shows a rough surface due to the presence of micronized mineral crystals (Figure 2b). Figure 2c,d illustrates the uniform coating of nanosized n-PBDF particles on the glass slides and rough black paint surfaces, respectively. Atomic force microscopy (AFM) images further corroborated the uniform nano-features of the n-PBDF particles ranging from 22 to 42 nm, with an average size of around 28 nm (Figure 2e and Figure S1, Supporting Information). The nanoscale size of the particles significantly reduces visible light scattering, enabling high visible transmittance. Additionally, attenuated total reflectance Fourier transform infrared spectroscopy was employed for qualitative analysis of the surface chemistry across four distinct samples (Figure 2f). The commercial black paint layer constitutes several fillers, adhesives, pigments, and other ingredients that result in the formation of strong peaks at 1720 cm^{-1} (C═O stretching of ester/carboxyl groups), 1165 and 1074 cm^{-1} (Si-O stretching), and various symmetric and asymmetric absorption bands. The n-PBDF film has shifted or new absorbance peaks at 1790 and 1630 cm^{-1} and within 1970–2160 cm^{-1}. Note that the 1790 cm^{-1} peak is ascribed to asymmetric C═O band stretching and is a spectral fingerprint for a 5-member lactone moiety. The clear spectral fingerprints of the two layers and the compatibility between the n-PBDF coating and paint layer, as well as the formation of the low-e paint, can be indirectly confirmed by the distinct stretching absorbance peaks observed when the n-PBDF film coexists with the low-e paint layer.

Figure 2g shows a clear absorbance spectrum of the n-PBDF ink solution in the UV–vis-NIR region. Despite being diluted more than 20-fold, the solution exhibited a distinct polaronic absorption that gradually increased in the NIR region. Both wavelength peaks, 487 and 1350 nm, across varying dilution concentrations showed a linear fit of absorbance with concentration. This trend is in accordance with the Beer–Lambert law, confirming the presence of extinction coefficients that correlate with the concentration of the n-PBDF ink solution (Figure S2, Supporting Information). Dynamic light scattering analysis was employed to determine the size distribution of the n-PBDF features within the ink solution, revealing an average hydrodynamic diameter of 76 nm. This result, detailed in Figure S3 (Supporting Information), attests to the uniform and stable dispersion of n-PBDF features within the solvent, emphasizing the suitability of ink for applications requiring uniform distribution and consistent performance across various substrates and paint layers.

2.3. Optical Characterization of the Colored Low-E Paints

The optical properties of dual-layer paint with n-PBDF coatings of different thicknesses on top of an opaque black paint layer were investigated to reveal its functionality in reducing the thermal emittance of commercial paints. The reflectance spectra of the low-e black paint, commercial black paint, and pure n-PBDF nanoparticles coated on a glass slide are shown in **Figure 3a**. The commercial paint showed consistently low reflectance throughout the solar and thermal wavelengths. Specifically, an average

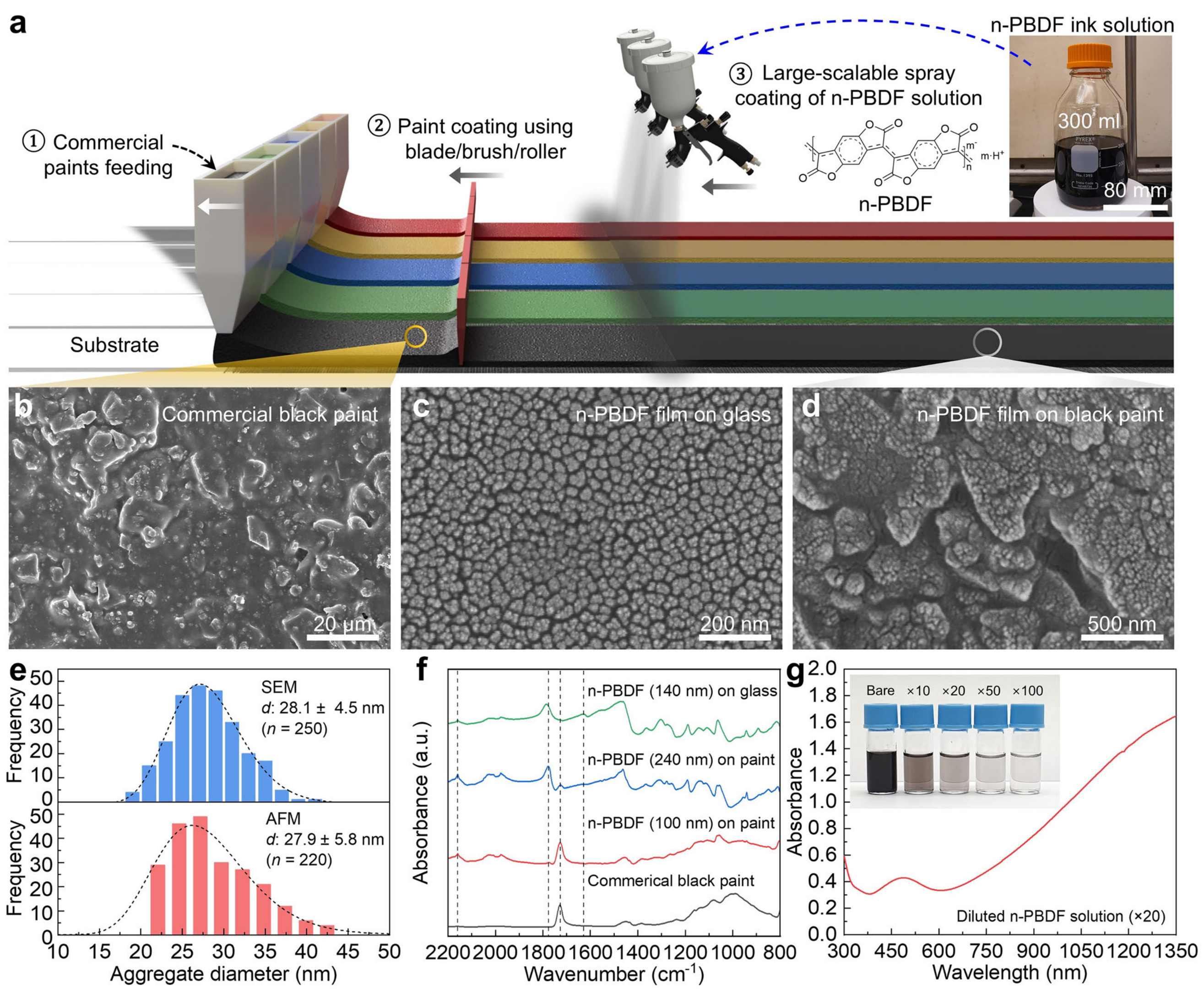

Figure 2. Schematic and characterization of the low-emissive conductive polymer coating process. a) Schematic illustration of large-scale spray coating of n-PBDF ink onto various substrates pre-coated with commercial-colored paints. The inset shows the eco-friendly ethanol-based n-PBDF ink solution, suitable for easy scale-up. b–d) SEM images illustrating b) commercial black paint, c) n-PBDF film on glass, and d) n-PBDF film atop the black paint layer. e) Distribution of the diameters of nano-scale aggregate particles formed on n-PBDF film surface, with an upper panel from SEM c,d) and a lower panel from AFM phase image (Figure S1, Supporting Information), highlighting nano-particulate features with an average diameter ≈28 nm. f) ATR FT-IR spectra for four different films with glass/black-painted substrates. g) UV–vis-NIR absorption spectrum of n-PBDF ink diluted over 20-fold (inset: serial-diluted n-PBDF ink solutions).

thermal reflectance of 0.05 indicates that, in a hot climate, it barely rejects heat gains from the surroundings; conversely, in a cold climate, it loses heat to its surroundings, hence increasing the heating demand. In striking contrast, the glass slide coated with the 194 nm-thick n-PBDF particles shows a sharp rise of reflectance from 0.6 μm and reaches ≈0.95 over the MIR wavelengths. The reflectance of low-e black paint with the same 194 nm thick n-PBDF particle coating starts to rise from 0.8 μm and maintains a high reflectance of 0.81 in the MIR wavelength, equivalent to 0.19 emissivity (Note S2, Supporting Information). Therefore, adding the n-PBDF layer to commercial black paint simultaneously blocks NIR radiation from the sun and MIR radiation from the hot surroundings in hot summer, thereby reducing the cooling demand. Moreover, its radiation heat loss is suppressed in a cold climate due to its minimized emissivity. It is worth noting that the thermal emissivity of the dual-layer low-e paint was tunable by varying the thickness of the n-PBDF top layer (Figure 3b). As it increased from 121 to 194 nm, the thermal reflectance elevated from 0.60 to 0.72, indicating a reduction in the thermal emissivity, which is visualized in the IR thermal images (Figure 3b, inset). In the naked eye, the visible colors of these low-e paints were very similar, but their corresponding IR thermal images showed a distinct reduction of "apparent temperature" from left to right due to reduced thermal emission as the n-PBDF layer thickness increased. The low-e paint with the thickest n-PBDF top coating shows the lowest surface temperature in the IR thermal image (See Experimental Section and Figure S4, Supporting Information, for more details).

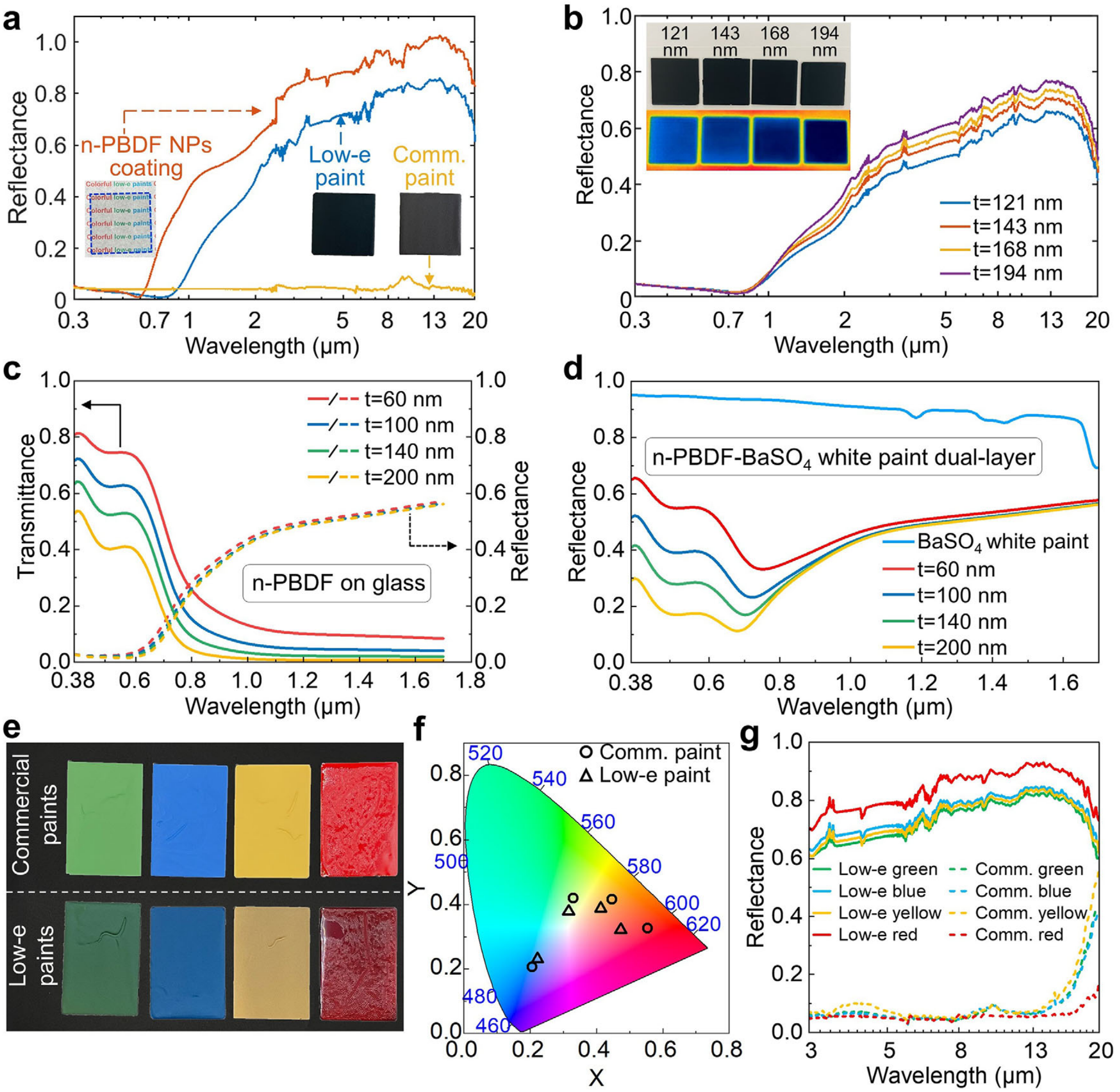

Figure 3. Tunable optical properties of the low-e paint in the solar and MIR wavelengths. a) Reflectance spectra of low-e black paint, n-PBDF, and commercial black paint. The inset shows their photographs, and all the samples were coated on glass. b) Reflectance spectra of low-e black paints with various n-PBDF coating thicknesses. The inset shows their photos and corresponding IR images. c) Simulated transmittance and reflectance spectra of the n-PBDF coatings of various thicknesses coated on the glass slide. d) Simulated reflectance spectra of the low-e black paint with n-PBDF coatings of various thicknesses on top of an opaque $BaSO_4$-acrylic radiative cooling paint.[43] e) Photographs showing the commercial-colored paints and the dual-layer low-e counterparts. f) Chromaticity of the commercial paints (circle markers) and the corresponding low-e paints (triangle markers) with different colors are shown in the CIE 1931 color space. g) The Reflectance spectra of commercial paints (solid curves) and the low-e paints (dashed curves) in the MIR region.

Simulating the optical properties of n-PBDF coating layers with different thicknesses is important for engineering optimal low-e paints' design. Figure S5 (Supporting Information) compares the simulated versus measured reflectance and transmittance of a 168 nm-thick n-PBDF coating on a 1 mm-thick glass slide. Since the mean particle size of 27.4 nm is considerably less than the wavelength, the scattering coefficient is negligible. This simplifies the problem to a homogeneous absorbing medium, with Fresnel's equations accounting for specular reflection and the Beer–Lambert law accounting for absorption within the n-PBDF coating and glass slide.[42] The simulation implies that the high transmittance in the visible spectrum is due to the low refractive index and extinction coefficient, while the reflectance increases toward the NIR region because the extinction coefficient greatly increases, causing enhanced boundary scattering at the top surface. Figure 3c shows the simulated spectral response for four different n-PBDF coating thicknesses. The reflectance curve is almost identical for all four thicknesses, which is due to the large extinction coefficient that induces a high boundary reflectance at the top surface and the high absorption of light that penetrates the film. This shows the behavior of conducting materials and explains why the coating is very effective even at low thicknesses because reflectance occurs on the top surface and not because of diffuse volumetric scattering throughout the nanoparticle coating, which requires a certain thickness to be effective. Figure 3d compares the simulated reflectance of a $BaSO_4$-acrylic radiative cooling paint with no top coat versus four different thicknesses of n-PBDF coatings.[43] The multi-layer structure was simulated with Monte Carlo simulations using the open-source code FOS.[44] We see here again that the reflectance in the NIR is dominated by the n-PBDF's large extinction coefficient through the NIR; however, the visible reflectance of the paint varies because the lower extinction coefficient in this spectrum does not induce as much boundary reflection while still absorbing the light passing through it before reaching the $BaSO_4$-acrylic bottom layer.

Versatility in design is another critical attribute of our low-e paint, which offers designers a broad range of aesthetic options. The dual-layered structure of our low-e paints allows us to use the same n-PBDF-composed top layer on commercial paints of various colors. The top panel of Figure 3e shows green, blue, yellow, and red commercial paints on glass slides, while the bottom row shows them with a 143 nm-thick n-PBDF layer. The low-e paints had a slightly darker color than the bare paints, as reflection peaks were weakened (Figure S6, Supporting Information). As depicted in Figure 3f, the commercial-colored paints and our low-e versions have similar chromaticity coordinates in the chromaticity diagram based on the CIE 1931 color space, suggesting that the addition of the n-PBDF layer does not significantly alter the perceived color of the base-layer paint. Moreover, commercial paints are closer to the edge of the diagram, representing more saturated colors than low-e paints.[45] Over the MIR wavelengths, the reflectance spectra of the low-e paints showed trends similar to those of the n-PBDF layer alone (Figure 3g). Taking blue as an example, the MIR reflectance of the commercial blue paint was only 0.10, whereas that of the low-e blue paint was as high as 0.80, which is an eight-fold enhancement (Figure S7, Supporting Information).

2.4. Theoretical Thermal Responses of the Low-E Paints in Hot and Cold Climates

The heat transfer process between buildings and their surroundings, including a neighboring object and the ground, is illustrated in **Figure** 4a, highlighting the advantage of low-e paints in stabilizing building temperatures compared with commercial paints in varying climatic conditions. First, the building wall can dissipate thermal energy to outer space via spontaneous thermal radiation (P_{rad}). The thermal energy transfer between the neighboring object and the building wall includes direct thermal radiation (P_{n_d}) and thermal radiation (P_{n_r}) reflected by the ground. Similarly, the building wall also exchanges thermal energy with the atmosphere in two paths: direct thermal radiation (P_{a_d}) and thermal radiation (P_{a_r}) reflected by the ground. There is also heat exchange of direct thermal radiation (P_g) between the building wall and the ground. Moreover, the building wall can directly dissipate thermal radiation to outer space (P_{rad}). The thermal equilibrium equation to access the surface temperature of the building facing a neighboring object and underlying ground is described as $P_{rad}(T_{wall}) - P_{sun} - P_a - P_n - P_g + P_{conv} = 0$. The computed wall temperatures for buildings coated with low-e paint and commercial paint facing a neighboring object in hot and cold climates are illustrated in Figure 4b,c, respectively. The surface emissivity of the neighboring object was set to 0.9, which is the most common building envelope for bricks, concrete, and paint. A distance of 25 m between these two items was selected to simulate the urban building layout. Both buildings had the same height of 50 m and were aligned with a 15-story building. The ground between them has an emissivity of 0.9, with the assumed construction material of asphalt.[46] More details about the calculation can be found in Note S3 and Figure S8, Supporting Information.

A wall coated with low-e paint can stabilize its temperature in both hot and cold climates. Figure 4b demonstrates that in a hot climate with an ambient temperature of 30 °C and a road surface temperature of 60 °C, the low-e paint-coated wall (low-e wall) demonstrates a flat response to significant fluctuations in the neighboring object temperature compared with the commercial paint-coated wall (commercial wall). This characteristic prevents large temperature variations in building walls from regulating indoor temperatures and enhancing thermal comfort. Specifically, when the neighboring object's temperature exceeded 57 °C, the low-e wall showed a lower surface temperature, outperforming the commercial wall. This outcome arises because when the neighboring object has a relatively lower surface temperature (below 57 °C), the wall's absorption of radiation from the surroundings is limited compared to the thermal emission from the wall to outer space; therefore, both the commercial wall and low-e wall exhibit a subambient surface temperature. Under such circumstances, owing to the high emissivity of the commercial wall in the MIR, it exhibits superior cooling performance by dissipating more thermal energy and providing a lower surface temperature than the low-e wall. However, when the surrounding objects exceed 57 °C, the commercial wall absorbs a significant amount of the incoming thermal irradiation, thereby offsetting and even surpassing the heat dissipated into outer space. In contrast, the low-e wall effectively rejected this incoming thermal energy and helped maintain a stable temperature (Figure S9, Supporting Information). In parallel, the temperature regulation performance of the wall in a cold climate is shown in Figure 4c. The ambient and road surface temperatures were both set to 5 °C. Regardless of the varying temperatures of the neighboring object, ranging from −35 to 25 °C, the low-e wall consistently maintained a higher temperature than the commercial wall. This is because, even in cold climates, commercial walls with high surface emissivity dissipate thermal energy to outer space and cold surroundings, increasing the heating load on the building (Figure S10, Supporting Information).

2.5. Indoor Thermal Performance of Low-E and Commercial Paints

The temperature response of low-e paint and commercial paint under controlled hot and cold conditions extensively highlights the capability of low-e paints in reducing temperature fluctuations compared to commercial paints (Figure 4d–i). Figure 4e displays the continuous hourly temperature response of low-e black paints with n-PBDF coating thicknesses of 143, 194, and 231 nm on commercial black paint and pristine commercial black paint with a size of 35 × 35 mm. All samples exhibited a temperature increase, with the commercial paint showing the highest

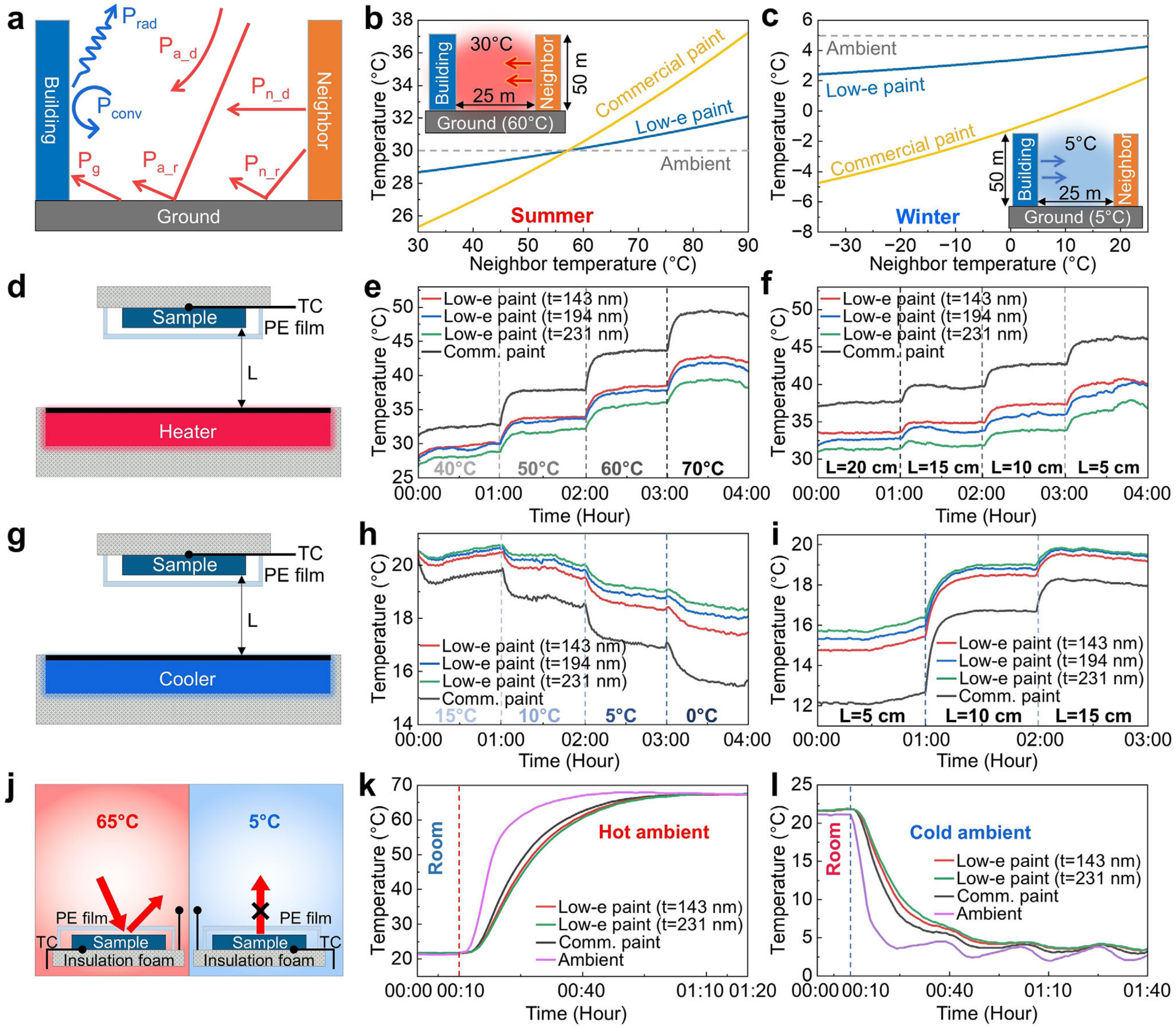

Figure 4. Demonstration of thermal regulation for low-e paint in artificial hot and cold environments. a) Schematic illustrating the heat exchange process between two building walls. b,c) Calculated surface temperatures of walls coated with low-e black paint and commercial black paint as a function of the neighboring building surface temperatures b) in summer and c) in winter. The inset displays a simplified layout of the walls and ground. d) Experimental setup of temperature response for low-e paints and commercial black paints facing a hot plate. e,f) The measured temperature of low-e black paints with different n-PBDF coating thicknesses compared to commercial black paint when e) the hot plate temperature increased from 40 to 70 °C and f) the distance between samples and the hot plate changed from 20 to 5 cm. g) Experimental setup when paint samples faced a cold plate. h,i) The measured temperature when h) the cold plate temperature changes from 15 to 0 °C and i) the distance between the samples and the cold plate changes from 15 to 5 cm. j) Schematic of the temperature response in hot (left) and cold (right) environments. k,l) Transient temperature responses of low-e and commercial black paints after transfer to k) hot and l) cold environments, respectively.

temperature increase from ≈32.5 to ≈49.4 °C, while all samples with low-e paints exhibited a lower temperature increase. The low-e paint with a 231 nm-thick n-PBDF coating layer (i.e., our sample with the highest thermal reflectance) exhibited the lowest temperature increase, further demonstrating the efficiency of our low-e paint in suppressing thermal energy uptake from the surroundings (Figure S11, Supporting Information). The temperature responses of the samples when the heating plate was fixed at 60 °C and the distance was varied from 20, 15, 10, to 5 cm are shown in Figure 4f. The temperature profiles of all the samples exhibited an increase as the heating distance decreased. This indicates that the heat rejection effect of the low-e paints became more pronounced as they approached the heating source. As expected, the commercial paint consistently surpassed that of the low-e samples throughout the test. We also recorded temperature variations to study the paints' indoor thermal performance when facing a cooling source. Figure 4h reveals that when the temperature of the cooling source decreased while the cooling distance between the samples and the cooling plate was fixed at 10 cm, the temperature of all samples progressively declined.

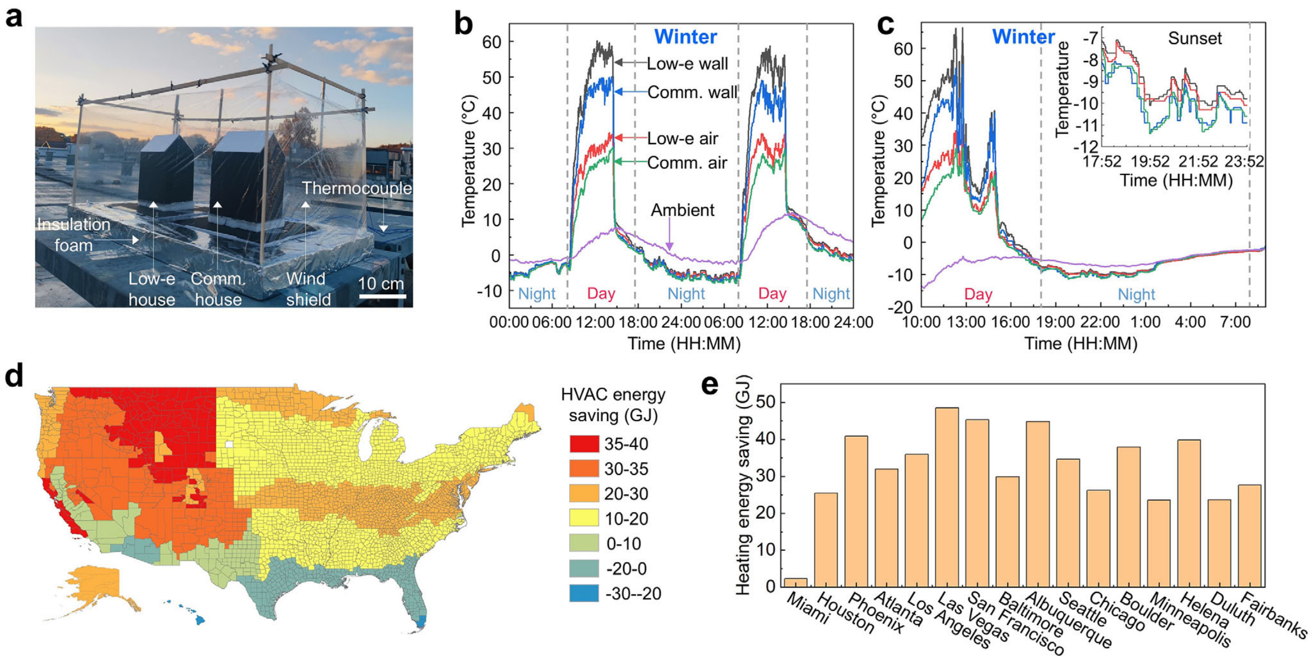

Figure 5. Field tests and energy-saving estimations. a) Photograph showing the experimental setup for the thermal regulation capacity. b,c) Temperature of the wall and interior air during the 2-day field test. The inset shows the temperature measured after sunset. d) Simulated HVAC energy-savings map for a midrise apartment building across the United States with low-e paint. e) Estimated annual heating energy savings for a mid-rise apartment building in 16 representative cities.

Due to the high thermal emissivity of commercial paint, it experiences the largest temperature reduction. The low-e paints with increasing n-PBDF layer thickness exhibited smaller temperature drops, indicating that the low-e paint can effectively retain the temperature when faced with a cooler object (Figure S12, Supporting Information). In Figure 4i, the temperature profiles of all the samples were recorded, beginning with a distance of 5 cm and a fixed cooling temperature of 0 °C. The surface temperatures of all samples increased as the cooling distance increased to 10 cm and subsequently to 15 cm. As more thermal energy is lost from commercial paints, they always display a much lower temperature than low-e paints at all cooling distances. Among the low-e paints, the one with the thickest coating layer with lower thermal emissivity showed the best temperature regulation effect, with a minimal temperature drop when facing a cooling source.

To further study the transient thermal performance of the paints, an environmental box was established to simulate ambient temperatures of 65 and 5 °C, respectively (Figure 4j). The temperature responses of commercial paint and low-e paint with n-PBDF coating thicknesses of 143 and 213 nm, respectively, on glass slides were monitored. All samples were first stabilized at room temperature after temperature recording for 10 min and then transferred to an environmental box for continuous temperature recording. As shown in Figure 4k,l, after these paints were exposed to hot or cold environmental boxes, commercial paints showed a faster response of either increasing or decreasing temperature. Low-e paints experienced slower temperature changes before eventually reaching thermal equilibrium with the environment due to their small thermal exchange with the surroundings.

2.6. Thermal Stabilization and Energy-Saving Performance of Low-E Paints

To investigate the thermal maintenance performance of low-e paint in practical applications, field tests were conducted during winter on the rooftop of a three-story building at Purdue University, West Lafayette, IN, USA. The experimental setup is shown in **Figure 5a**. In the field test, two structurally identical house models were built using the same wooden sheets painted with black walls and a white roof. The walls of one house were coated with commercial black paint, called a commercial house, and those of the other house were coated with low-e black paint, called a low-e house. The thermal emissivity values for the commercial house wall and low-e house wall are 0.95 and 0.31, respectively. To minimize the heat transfer effect from the roof and bottom of the houses, allowing us to maximize the thermal performance of the walls, the roofs were painted with ultra-white $BaSO_4$ paint with a solar reflectance of 97%,[43] and the bottoms of the houses were sealed with insulating foam. Thermocouples were affixed to the inside surface of the wall and the central point of the indoor space for each house at identical positions to capture the wall and interior air temperatures. In the field test, two houses were placed in parallel on a thermal insulation foam wrapped in aluminum foil, with the walls holding the thermocouples on the inner face facing eastward. Moreover, a windshield with a MIR-transparent film was employed to obtain a controlled and consistent environment with similar convection coefficients during the measurements (Note S4, Supporting Information). Figure 5b shows the test results over two consecutive days from Dec. 13th to Dec. 14th, 2023, with the highest daytime ambient temperature of 12 °C and the lowest nighttime ambient temperature of

≈3 °C. During these two clear days, changes in the wall and air temperatures inside the houses generally followed the ambient temperature trend, but under the influence of solar irradiation. It was observed that the average temperature for the low-e paint-coated wall (low-e wall) exceeded that of the wall coated with commercial paint (commercial wall) by ≈9.1 °C from 11:00 to 14:00 on Dec. 13th (Figure S13c, Supporting Information). Meanwhile, the average air temperature within the low-e house was recorded to be 4.3 °C higher than that within the commercial house during the same time interval. This difference in thermal performance highlights the photothermal regulation advantages of our low-e paint. While the solar energy absorbed by the low-e paint is comparable to that of the commercial black paint, the thermal radiation loss is markedly lower for the low-e paint. Quantitative analysis of the reflectance and emittance spectra of the low-e black paint and the commercial black paint under a solar intensity of 500 W m^{-2} revealed only minor differences in visible light absorption (3.44 W m^{-2}) and NIR absorption (29.4 W m^{-2}). However, the thermal radiation loss for the low-e paint was reduced by 465.3 W m^{-2} for an object at 50 °C (the average wall temperature for these two paints between 11:00 and 13:00). The thermal performance of the low-e paint is particularly evident in cold climates. On Jan. 21st, 2024, a day characterized by high solar intensity, a maximum daytime ambient temperature of −5 °C, and a minimum nighttime ambient temperature of −18 °C, the average wall temperature of the low-e house between 11:00–12:00 noon was 7.0 °C higher than that of the house coated with commercial black paint (Figure 5c). Furthermore, the average interior air temperature of the low-e house was 6.1 °C warmer than that of the commercial house (Figure S13d, Supporting Information). At night, without external heat input, both the low-e and commercial houses dissipated large amounts of thermal energy to the environment, with interior temperatures falling below the ambient temperature. More importantly, the low-e house limited radiative heat loss from the house to the cold environment, retaining higher thermal energy within the building. Therefore, even at night, the equilibrium temperature of a low-e house remained relatively high (Figure 5c, inset). After 2:00 AM, as the weather became cloudy, thermal dissipation through radiative heat transfer to outer space was suppressed. Under these conditions, heat exchange between the house and the environment was primarily governed by convection and conduction. Therefore, the temperatures of the low-e house and commercial house gradually converged and eventually reached equilibrium with the ambient temperature.

2.7. Energy-Saving Potential for Building Envelope Applications

The building energy simulation software, EnergyPlus, was applied to evaluate the HVAC energy-saving performance by coating the low-e paints on a reference building wall of a post-1980 midrise apartment (See Experimental Section; Figure S14 and S15, Supporting Information for more details). The annual total energy savings of the HVAC system in 16 representative cities in the United States spanning different climate zones are shown in Figure 5d. Our low-e paint saves energy in most climate zones. The northern regions, characterized by extended periods of cold and dry climates, display the most substantial energy savings. This can be attributed to the heating demand dominating over cooling demand in these regions, and our low-e paint can reduce heat loss from the building walls (Figure 5e). For instance, in Fairbanks, Alaska, it is estimated that our low-e paint can yield an annual HVAC energy-saving of 26.4 GJ. Additionally, in mild and humid climates, such as Seattle, our low-e paint still maintains energy savings of 30 GJ annually. On the other hand, in some climate zones with high humidity and temperature, such as Miami and Phoenix, substantial air conditioning and air circulation are required, and our low-e paints did not show the expected energy savings. This could be attributed to the constraints of the EnergyPlus software in accounting for ground temperature increases and their associated mid-infrared radiation, as well as the lack of insulation material modeling for buildings in the southern United States in EnergyPlus. During summer, solar radiation raises ground temperatures, leading to substantial mid-infrared radiation that contributes to the thermal load on building walls. However, the thermal regulation advantage of low-e paint in mitigating ground thermal emission was not captured in the final energy saving.

3. Conclusion

In conclusion, this study demonstrates an innovative, scalable, and durable colored low-e paint that features a dual-layer structure comprising an ultrathin top n-PBDF coating layer and a colored commercial paint base layer, achieving significant thermal regulation while preserving the aesthetic appearance. Being a transparent organic conductor, a thin 200 nm-thick top coating of n-PBDF on commercial paints suppresses the emissivity from 0.95 to 0.19. Moreover, the coating thickness of the top n-PBDF layer can be adjusted to tune the thermal emissivity of the resulting paint, indicating significant flexibility in the thermal regulation and design of low-e paints. In winter, the low-e wall was 9.1 °C warmer than the wall coated with commercial black paint (black wall) during noontime. Our low-e paint can effectively reject thermal radiation from neighboring buildings and surroundings in hot climates while reducing thermal radiation loss in cold climates, enabling radiative thermal regulation of buildings, enhancing thermal comfort, and saving energy. The EnergyPlus simulation estimates that our low-e paint could lead to significant annual energy savings across most U.S. climate zones for a typical midrise apartment, such as San Francisco (39 GJ, or 10833 kWh), Chicago (20 GJ, or 5556 kWh), and Fairbanks (26.4 GJ, or 7333 kWh). Moreover, our low-e paint is compatible with common application techniques, such as spraying and brushing, and can adapt to diverse surface geometries, ensuring easy integration into existing building practices, thus lowering installation costs and facilitating widespread adoption. This approach marks a significant advancement in energy-efficient building envelopes, enhancing thermal stabilization without sacrificing design aesthetics.

4. Experimental Section

Fabrication of Colorful Low-e Paint Films: Commercial onyx black paint provided by Tex-Cote LLC and green, blue, yellow, and red paints from Rust–Oleum were applied to glass substrates (5.0 × 7.5 cm, Corning Inc. US) using a custom home-built blade coating, followed by drying under ambient conditions for 4 h to form color-painted films. The n-type conducting polymer, n-PBDF, was synthesized in DMSO solvent through a one-pot synthesis, as previously described.[40] To prepare the low-e n-PBDF ink solution, dialyzed n-PBDF (<10 K molecular weight cutoff, cellulose membrane dialysis tubing, Fisher Scientific) was gradually added to stirred anhydrous ethanol (200 proof, 100% undenatured, Fisher Scientific) at a 1:6 (v/v) ratio, ensuring a homogeneous dispersion. The mixture was gently stirred at room temperature for 2 h, maintaining dispersion stability for over two weeks. Uniform low-e n-PBDF films were fabricated using an ultrasonic spray coating system (ExactaCoat, Sono-Tek Inc.), achieving thicknesses exceeding 100 nm. A 120 kHz ultrasonic spray nozzle (Impact, Sono-Tek) was operated at a liquid flow rate of 0.5 mL min^{-1} and nozzle-to-substrate distance of 50 mm, following an arc-shaped pattern with automated repeated cycling. To ensure reliable structural modeling and high experimental reproducibility, the film thickness precision (less than ±3% standard deviation) was evaluated using a surface profiler (DektakXT, Bruker) by measuring at least five points across different batches of glass substrates under identical coating conditions.

Characterization: For the optical characterization of the n-PBDF ink solution prepared through a series dilution method at various concentrations (10-, 20-, 50-, and 100-fold), 3 mL of each solution was used in a cleaned quartz liquid cell (light path length: 1 cm). UV-vis-NIR absorption spectra were recorded using an Agilent Cary 5000 UV–vis Spectrometer. Absorbance FT-IR spectra were measured using a Nicolet 6700 FT-IR spectrometer (Thermo Nicolet Corp.) equipped with an Attenuated Total Reflectance (ATR) Smart iTR accessory, utilizing a single-bounce diamond crystal, across a wavenumber range of 4000 to 800 cm^{-1}, with a spectral resolution of 4 cm^{-1} and an averaging of 64 scans. Baseline correction and maximum peak normalization were performed without additional smoothing using the OMNIC software (v.8.3, Thermo Nicolet Corp.).

For the optical characterization of low-e paints prepared with colorful commercial paint as the base layer, the paints were painted on the glass slide as the substrate. The total hemispheric transmittance and reflectance spectra from 0.3 to 2.5 µm were measured by an ultraviolet-visible-near-infrared (UV-vis-NIR) spectrometer with an integrating sphere and a certified Spectralon diffuse reflectance standard (Lambda 950, Perkin Elmer, Inc., USA). A Nicolet iS50 FTIR spectrometer with a PIKE Technologies integrating sphere was used to measure the total hemispheric transmittance and reflectance between 2.5 and 20 µm. Kirchhoff's law and the thermal equilibrium principle were used to derive the emittance (ε) spectrum based on the measured reflectance (r) and transmittance (t) spectra, where $\varepsilon = 1 - r - t$. SEM images were taken with Hitachi S-4800 Field Emission SEM.

Thermal Measurements: All IR thermal images were recorded using a thermal camera (FLIR E8xt). For the IR thermal image of low-e black "P" and the commercial black paint background in Figure 1f, all paints were coated on an aluminum plate working as the substrate. The plate was fixed to a vertical brick wall facing southwest. The IR thermal image was taken using the thermal camera after 30 min of natural sunlight exposure. For the IR thermal image of low-e black paints with different n-PBDF coating thicknesses shown in Figure 3b, all paints were applied to 1 mm-thick glass slides in the dimension of 3 × 3 cm, working as substrates. These samples were placed on a hot plate covered with a black metal plate, which has a surface emissivity of 0.94. The temperature of the hot plate was set to 60 °C. After the temperature stabilized, the IR thermal image was captured using a thermal camera at room temperature. For the indoor thermal regulation demonstration tests shown in Figure 4, all temperatures of samples were measured by T-type thermocouples. For the outdoor field tests shown in Figure 5a–c, the temperatures of the house wall and inside air were measured by K-type thermocouples.

Indoor Test Temperature Response Characterization: For the indoor test to examine the temperature response of low-e black paints and commercial black paint facing a hot plate and cold plate, three different low-e black paint samples with n-PBDF coating thicknesses of 143, 194, and 231 nm, respectively, were prepared, and commercial black paint was used as the control group. All paints were coated on a glass slide with dimensions of 35 × 35 × 1 mm as the substrate. T-type thermocouples were used to measure the real-time temperature of the samples, affixed to the backside of each glass slide, and secured onto an expansion polystyrene foam enveloped by a highly reflective foil, serving as an adiabatic background for the samples. Additionally, to minimize the influence of ambient airflow on the sample temperature, a MIR-transparent polyethylene (PE) film was applied over the top area of the samples, allowing a specific concentration on radiative heat transfer. A temperature-adjustable plate was placed under the samples and covered with a black metal plate with a surface emissivity of 0.94. For the temperature response tests when the samples faced a heating source, as discussed in Figure 4d–f, a hot plate worked as the heating source with adjustable temperatures from 40, 50, 60, to 70 °C, and the heating distances between the black metal plate and the sample could be changed from 20, 15, 10, to 5 cm. For the temperature response tests when samples faced a cooling source, as discussed in Figure 4g–i, a thermoelectric cooler-controlled-plate worked as the cooling source with adjustable temperatures from 15, 10, 5, to 0 °C, and the cooling distances between the black metal plate and the sample can be changed from 5, 10, to 15 cm.

Building Energy Saving Calculation: EnergyPlus was used to estimate year-round HVAC energy consumption. Utilizing a reference building model of a post-1980 midrise apartment, as defined by the U.S. Department of Energy, the study incorporated a 500 µm-thick low-e paint on the exterior surface of the walls (Table S1, Supporting Information). To minimize the variations in energy consumption assessments attributable to the different color appearances of the building walls, the optical properties in the solar spectrum were maintained to align with the appearance of the original reference building model. This study specifically focused on the optical properties in the MIR wavelength range through the application of low-e paints. In the simulation, the MIR thermal emissivity of the wall coated with low-e paint was set as 0.2, while the default value for the reference building wall was 0.9. To consider the impact of the thermal and optical properties of the surrounding objects on the studied building, in the simulation model, the studied building was placed amid four identical apartments surrounding it at a distance of 15 m. To ensure a comprehensive evaluation, Sixteen representative cities across various climate zones in the U.S. were encompassed, including Miami, Houston, Phoenix, Atlanta, Los Angeles, Las Vegas, San Francisco, Baltimore, Albuquerque, Seattle, Chicago, Boulder, Minneapolis, Helena, Duluth, and Fairbanks. For each location, hourly weather data for a typical meteorological year (TMY3) were employed as the basis for external weather conditions, incorporating variables such as temperature, relative humidity, wind speed, and solar radiation. The HVAC system included heating (for both electricity- and natural gas-powered ways), cooling, and fans, and the HVAC energy consumption was calculated for a pristine building with conventional building walls and those coated with the low-e paint, respectively.

Supporting Information

Supporting Information is available from the Wiley Online Library or from the author.

Acknowledgements

X.L. acknowledges the Gilbreth Postdoctoral Fellowship at Purdue University. W.-J.L., L.Y., and J.M. acknowledge the support from Ambilight Inc. under contract #4000187.02. J.R. acknowledges the support from the Center for Soft PhotoElectroChemical Systems, an Energy Frontier Research funded by Department of Energy, Office of Science, Basic Energy Sciences, under award #DE-SC0023411. D.W.C. and X.R. acknowledge partial support from the US National Science Foundation through award 2102645, A.F. and O.G.R.G. acknowledge support from the US National Science Foundation through a Graduate Research Fellowship. Q.G. and Y.L. are partially supported by KAUST (BAS/1/1415-01-01) and FutureWei's gift fund: radiative cooling and thermal management materials for consumer electronics (GIF/5/5705-01). A.A. acknowledges the support from Saudi Arabian Cultural Mission (SACM).

Conflict of Interest

A provisional patent (file number: 63/794,705) based on this work was filed with the U.S. Patent and Trademark Office on April 25, 2025. J.M. is a cofounder of Ambilight.

Author Contributions

X.L. and W.-J.L. contributed equally to this work. X.R. and J.M. conceived the idea and supervised the project. X.L. and W.-J.L. fabricated the samples, validated the results, visualized the data, and wrote the first draft. W.-J.L. conducted the synthesis, scalable fabrication, and characterizations with the help of J.R. and L.Y. X.L. and Y.T. conducted thermal modelling, designed and carried out indoor measurements and field tests. D.W.C. conducted the optical simulation. A.F., Z.X., O.G.R.G., and A.A. performed material characterizations. Y.L., Y.T., and Q.G. conducted the EnergyPlus simulation. The manuscript was written through the contributions of all authors. All authors have given approval to the final version of the manuscript.

Data Availability Statement

The data that support the findings of this study are available from the corresponding author upon reasonable request.

Keywords

HVAC energy-saving, low-emissivity paint, n-PBDF, organic conducting polymer

Received: October 16, 2024
Revised: February 25, 2025

---

[1] I. Hamilton, O. Rapf, D. J. Kockat, D. S. Zuhaib, T. Abergel, M. Oppermann, M. Otto, S. Loran, I. Fagotto, N. Steurer, *United Nations Environ. Program* **2020**.
[2] L. Pérez-Lombard, J. Ortiz, C. Pout, *Energy Build.* **2008**, *40*, 394.
[3] S. D. Rezaei, S. Shannigrahi, S. Ramakrishna, *Sol. Energy Mater. Sol. Cells* **2017**, *159*, 26.
[4] R. H. Galib, Y. Tian, Y. Lei, S. Dang, X. Li, A. Yudhanto, G. Lubineau, Q. Gan, *Nat. Commun.* **2023**, *14*, 6707.
[5] Y. Tian, X. Liu, Z. Wang, J. Li, Y. Mu, S. Zhou, F. Chen, M. L. Minus, G. Xiao, Y. Zheng, *Nano Energy* **2022**, *96*, 107085.
[6] S. B. Sadineni, S. Madala, R. F. Boehm, *Renew. Sustain. Energy Rev.* **2011**, *15*, 3617.
[7] Y. Cui, Y. Ke, C. Liu, Z. Chen, N. Wang, L. Zhang, Y. Zhou, S. Wang, Y. Gao, Y. Long, *Joule* **2018**, *2*, 1707.
[8] S. Wang, Y. Zhou, T. Jiang, R. Yang, G. Tan, Y. Long, *Nano Energy* **2021**, *89*, 106440.
[9] J. Chai, J. Fan, *Adv. Energy Mater.* **2023**, *13*, 2202932.
[10] R. Zhang, R. Li, P. Xu, W. Zhong, Y. Zhang, Z. Luo, B. Xiang, *Chem. Eng. J.* **2023**, *471*, 144527.
[11] Z. Zhang, L. Zhang, Y. Zhou, Y. Cui, Z. Chen, Y. Liu, J. Li, Y. Long, Y. Gao, *Chem. Rev.* **2023**, *123*, 7025.
[12] B. P. Jelle, *Start-up creation*, **2016**, 129, 181.
[13] L. Aditya, T. M. I. Mahlia, B. Rismanchi, H. M. Ng, M. H. Hasan, H. S. C. Metselaar, O. Muraza, H. B. Aditiya, *Renew. Sustain. Energy Rev.* **2017**, *73*, 1352.
[14] A. Felicelli, J. Wang, D. Feng, E. Forti, S. El Awad Azrak, J. Peoples, J. Youngblood, G. Chiu, X. Ruan, *Nanophotonics* **2024**.
[15] X. Xue, M. Qiu, Y. Li, Q. M. Zhang, S. Li, Z. Yang, C. Feng, W. Zhang, J. Dai, D. Lei, *Adv. Mater.* **2020**, *32*, 1906751.
[16] X. Li, J. Peoples, Z. Huang, Z. Zhao, J. Qiu, X. Ruan, *Cell Rep. Phys. Sci.* **2020**, *1*, 100221.
[17] H. Bao, C. Yan, B. Wang, X. Fang, C. Y. Zhao, X. Ruan, *Sol. Energy Mater. Sol. Cells* **2017**, *168*, 78.
[18] X. Li, B. Sun, C. Sui, A. Nandi, H. Fang, Y. Peng, G. Tan, P. C. Hsu, *Nat. Commun.* **2020**, *11*, 6101.
[19] J. Mandal, Y. Fu, A. C. Overvig, M. Jia, K. Sun, N. N. Shi, H. Zhou, X. Xiao, N. Yu, Y. Yang, *Science* **2018**, *362*, 315.
[20] Y. Zhai, S. N. David, D. Zhao, R. Lou, G. Tan, R. Yang, *Science* **2017**, *355*, 1062.
[21] B. Zhao, C. Xu, C. Jin, K. Lu, K. Chen, X. Li, L. Li, G. Pei, *Nanophotonics* **2024**, *13*, 583.
[22] S. Y. Jeong, C. Y. Tso, Y. M. Wong, C. Y. H. Chao, B. Huang, *Sol. Energy Mater. Sol. Cells* **2020**, *206*, 110296.
[23] X. Li, J. Peoples, P. Yao, X. Ruan, *ACS Appl. Mater. Interfaces* **2021**, *13*, 21733.
[24] R. V. Ralegaonkar, R. Gupta, *Renew. Sustain. Energy Rev.* **2010**, *14*, 2238.
[25] H.-Y. Chen, C. Chen, *Constr. Build. Mater.* **2016**, *126*, 130.
[26] R. Wu, C. Sui, T. H. Chen, Z. Zhou, Q. Li, G. Yan, Y. Han, J. Liang, P. J. Hung, E. Luo, D. V. Talapin, P. C. Hsu, *Science* **2024**, *384*, 1203.
[27] S. Liu, C. Sui, M. Harbinson, M. Pudlo, H. Perera, Z. Zhang, R. Liu, Z. Ku, M. D. Islam, Y. Liu, R. Wu, Y. Zhu, J. Genzer, S. A. Khan, P. C. Hsu, J. E. Ryu, *Nano Letters* **2023**, *23*, 7767.
[28] J. Mandal, S. Mandal, J. Brewer, A. Ramachandran, A. P. Raman, *Cell Rep. Phys. Sci.* **2024**, 5.
[29] N. Wongsuntirad, P. Rakkwamsuk, W. Harnnarongchai, *Mater. Today Proc.* **2018**, *5*, 9603.
[30] K.-S. Chou, Y.-C. Lu, *Thin Solid Films* **2007**, *515*, 7217.
[31] Y. Peng, J.-C. Lai, X. Xiao, W. Jin, J. Zhou, Y. Yang, X. Gao, J. Tang, L. Fan, S. Fan, *Proc. Natl. Acad. Sci.* **2023**, *120*.
[32] Y. Peng, L. Fan, W. Jin, Y. Ye, Z. Huang, S. Zhai, X. Luo, Y. Ma, J. Tang, J. Zhou, L. C. Greenburg, A. Majumdar, S. Fan, Y. Cui, *Nat. Sustain.* **2022**, *5*, 339.
[33] G. Wu, D. Yu, *Prog. Org. Coatings* **2013**, *76*, 107.
[34] L. Yuan, X. Weng, L. Deng, *Infrared Phys. Technol.* **2013**, *56*, 25.
[35] N. Selvakumar, G. Karthik, S. Jayaraj, H. C. Barshilia, *Sol. Energy Mater. Sol. Cells* **2021**, *221*, 110906.
[36] Z. Wu, X. Wang, S. Hou, Y. Liu, Z. Tang, L. Yin, Y. Qiao, J. Wang, X. Liu, J. Mao, *Adv. Opt. Mater.* **2024**, *12*, 2301303.
[37] G. Liu, H. Hsu, S. Samal, W. Lee, Z. Ke, L. You, B. M. Savoie, J. Mei, *Angew. Chem.* **2024**, *137*.
[38] Y. Wang, X. Li, C. Wang, X. Jian, L. Zong, J. Wang, *Polym. Eng. Sci.* **2022**, *62*, 1941.
[39] Z. Li, W. Chen, *Mater. Chem. Front.* **2021**, *5*, 6315.
[40] Z. Ke, A. Abtahi, J. Hwang, K. Chen, J. Chaudhary, I. Song, K. Perera, L. You, K. N. Baustert, K. R. Graham, *J. Am. Chem. Soc.* **2023**, *145*, 3706.
[41] H. Tang, Y. Liang, C. Liu, Z. Hu, Y. Deng, H. Guo, Z. Yu, A. Song, H. Zhao, D. Zhao, *Nature* **2022**, *611*, 271.
[42] M. Born, E. Wolf, Elsevier **2013**.
[43] X. Li, J. Peoples, P. Yao, X. Ruan, *ACS Appl. Mater. Interfaces* **2021**, *13*, 21733.
[44] D. Carne, J. Peoples, Z. Guo, D. Feng, Z. Han, X. Liu, X. Ruan, *Comput. Phys. Commun.* **2024**, *307*, 109393.
[45] R. M. Al-saleem, B. M. Al-Hilali, I. K. Abboud, *J. Appl. Math.* **2020**, *1*, 4640175.
[46] E. Barreira, R. M. S. F. Almeida, M. L. Simões, *Sensors* **2021**, *21*, 1961.

Supporting Information

High-Performance Low-Emissivity Paints Enabled by N-Doped Poly(benzodifurandione) (n-PBDF) for Energy-Efficient Buildings

Xiaojie Liu,[†] Won-June Lee,[†] Daniel William Carne, Yanpei Tian, Andrea Felicelli, Yue Lei, Joseph A. Romo, Liyan You, Zixin Xiong, Orlando Gabriel Rivera Gonzalez, Abdulrahman Aljwirah, Qiaoqiang Gan, Jianguo Mei,[*] and Xiulin Ruan[*]

Note S1. Materials and methods

Materials: All reagents for the synthesis, ink formulation, and characterization were purchased from Sigma Aldrich, Fisher Scientific, and Acros Organics and used without further purification unless otherwise mentioned. Dimethyl sulfoxide (DMSO, anhydrous) and ethanol (anhydrous, 200 proof, 100% undenatured) were purchased from Sigma-Aldrich and Fisher Scientific and used without any further purification. Commercial onyx black paint was purchased from Tex-Cote LLC. Commercial green, blue, and yellow paints were resilient exterior acrylic latex paints, which were purchased from Sherwin-Williams. The Ford red paint was purchased from Rust-Oleum (Farm& Implement Enamel Paint). The n-type doped PBDF was synthesized in DMSO, as described in a previous study[1]. Cellulose membrane dialysis bag tubing (10K MWCO, SnakeSkin^{TM}) and glass slides (Corning Inc. US) were purchased from Fisher Scientific with thermal conductivity of 0.8 W/m K and specific heat capacity of 840–880 J/kg K.

Low-e paint fabrication: Commercial paints of various colors were applied to glass substrates via custom home-built blade coating. These were then allowed to dry under ambient conditions for approximately 4 h to form color-painted films. To prepare the low-emissivity (low-e) n-PBDF ink solution, the synthesized n-PBDF solution, previously dialyzed to 10 kDa, was gradually added to stirred anhydrous ethanol at a 1:6 (v/v) ratio, ensuring a highly homogenous dispersion. The mixture was stirred at room temperature and 500 rpm for at least 2 h. This solution maintained its dispersion stability for more than two weeks. For the fabrication of uniform and precise low-e n-PBDF films, an automated ultrasonic spray coating system (ExactaCoat, Sono-Tek Corp., US) was used. The system provided uniform coatings exceeding 100 nm in thickness, utilizing a 120 kHz ultrasonic spray nozzle (Impact, Sono-Tek) with a liquid flow rate of 0.5 ml/min and nozzle-to-substrate distance of 50 mm, employing an arc-shaped pattern with repeated cycling. To ensure reliability and reproducibility, film thickness precision (standard deviation ±2%) was assessed using a surface profiler (DektakXT, Bruker). The measurements were conducted at a minimum of five points across different batches of glass substrates under identical coating conditions.

Characterizations: The surface roughness and the presence of nanoscale particulate features on the surface of the film were characterized using atomic force microscopy (AFM) (Dimension Icon, Bruker Inc.) in the ambient air at room temperature, employing tapping mode at a scan rate of 0.2 Hz over a measurement area of 2 μm × 2 μm. Statistical analysis of the diameter distribution of particulate features, identified from the AFM phase images, was conducted using the NanoScope Analysis software (v.3.0) with its particle analysis function ($n > 220$). Additionally, the statistical distribution of the diameter of the disjoint features was quantified using SEM images analyzed using ImageJ software (v.1.54) ($n > 250$). The hydrodynamic radius of the n-PBDF features, solvated and dispersed within the n-PBDF ink solution, was characterized by Dynamic Light Scattering (DLS) (DynaPro Nanostar 2, Wyatt Technology Corporation, US) without prior syringe filtration, using a homogeneous solution diluted to 0.015 mg/ml. All measurements were averaged from the data obtained from five replicates.

Optical characterizations: For the optical characterization of the n-PBDF ink solution prepared through a series dilution method at various concentrations (10-, 20-, 50-, and 100-fold), 3 ml of each solution was used in a cleaned quartz liquid cell (light path length: 1 cm). UV-VIS-NIR absorption spectra were recorded using an Agilent Cary 5000 UV-VIS Spectrometer (1 nm resolution). Absorbance FT-IR spectra were measured using a Nicolet 6700 FT-IR spectrometer (Thermo Nicolet Corp.) equipped with an Attenuated Total Reflectance (ATR) Smart iTR accessory, utilizing a single-bounce diamond crystal, across a wavenumber range of 4000 to 800 cm^{-1}, with a spectral resolution of 4 cm^{-1} and an averaging of 64 scans. Baseline correction and maximum peak normalization were performed without additional smoothing using the OMNIC software (v.8.3, Thermo Nicolet Corp.).

The total hemispheric transmittance and reflectance from 300 to 2500 nm were measured by an ultraviolet-visible-near-infrared (UV-Vis-NIR) spectrometer with an integrating sphere and a certified Spectralon diffuse reflectance standard (Lambda 950, Perkin Elmer, Inc., USA). A Nicolet iS50 FTIR spectrometer with a PIKE Technologies integrating sphere was used to measure the total hemispheric transmittance and reflectance between 2.5 and 20 μm. Kirchhoff's law and the thermal equilibrium principle were used to derive the emittance (ε) spectrum based on the measured reflectance (r) and transmittance (t) spectra, which is $\varepsilon = 1 - r - t$.

Note S2. Calculation of overall solar reflectance and infrared thermal emittance

The overall hemispherical solar reflectance, $\bar{R}$, is the function of wavelengths and incident angles, which is defined as[2]:

$$\bar{R}(\lambda,\theta,\Phi)=\frac{\int_{0.3\mu m}^{2.5\mu m} I_{sun}(\lambda,\theta,\Phi)R(\lambda,\theta,\Phi)d\lambda}{\int_{0.3\mu m}^{2.5\mu m} I_{solar}(\lambda,\theta,\Phi)d\lambda}$$

Where λ is the wavelength of the solar radiation, θ is the zenith angle, and Φ is the azimuth angle. I_{sun} is the incident solar intensity at AM 1.5 which is confined from 0.3-4.0 μm. Here, the integration interval is limited from 0.3 to 2.5 μm, covering over 99% power intensity of the solar intensity. $R(\lambda,\theta,\Phi)$ is the spectral directional reflectance.

The overall infrared thermal emittance, $\bar{\varepsilon}$, is also dependent on the wavelengths and incident angles, which is expressed as[2]:

$$\bar{\varepsilon}(\lambda,\theta,\Phi)=\frac{\int_{2.5\mu m}^{20\mu m} I_{bb}(\lambda,\theta,\Phi)[1-R(\lambda,\theta,\Phi)]d\lambda}{\int_{2.5\mu m}^{20\mu m} I_{bb}(\lambda,\theta,\Phi)d\lambda}$$

Where $I_{bb}(\lambda,\theta,\Phi)$ is the blackbody radiation intensity given by Planck’s law. It should be noted that all the spectra used in this work were measured at room temperature.

Note S3. Theoretical thermal performance for the studied building

A thermal model was developed to characterize the surface temperature of the studied building surface when it faced a neighboring object and an underlying ground. The thermal equilibrium equation for the studied building walls is expressed below[3]:

$$P_{rad}(T_{wall}) - P_{sun} - P_a(T_a) - P_n(T_n) - P_g(T_g) + P_{conv}(T_{wall}, T_a) = 0$$

Where $P_{rad}(T_{wall})$ stands for the radiative cooling power of the studied building wall with the surface temperature of T_{wall}. P_{sun} is the absorbed solar power intensity. $P_a(T_a)$ represents the absorbed thermal radiative power emitted from the ambient with the ambient temperature of T_a. $P_n(T_n)$ means the absorbed thermal radiative power from the neighboring object with the surface temperature of T_n. $P_g(T_g)$ is the absorbed thermal radiative power emitted from the ground with the surface temperature of T_g. $P_{conv}(T_{wall}, T_a)$ is the convective power between the ambient and the studied building surface.

$$P_{rad}(T_{wall}) = \int_0^{\pi}\int_0^{\pi}\int_0^{\infty} I_{bb}(T_{wall}, \lambda)\varepsilon'(\lambda, \theta)cos(\theta)sin(\theta)d\lambda d\theta d\Phi$$

Where $I_{bb}(T_{wall}, \lambda) = 2hc^2\lambda^{-5}/[exp(hc/\lambda k_B T_{wall}) - 1]$ defines the spectral radiance of blackbody at a certain temperature. Here, h is the Planck's constant, c is the light velocity, and k_B is the Boltzmann constant. $\varepsilon'(\lambda, \theta) = \frac{1}{\pi}\int_0^{\pi} \varepsilon(\lambda, \theta, \Phi)d\Phi$ is the averaged emissivity over the azimuth angle in the zenith direction for the building wall, and here, $\varepsilon(\lambda, \theta, \Phi)$ is the spectral emissivity of the studied building wall. The azimuth angle of a wall is defined in the range of 0 to π, excluding the angle of the back portion of the wall (π to 2π), which is not oriented towards the surrounding objects.

$$P_a(T_a) = P_{a\_d} + P_{a\_r}$$

$$= \int_0^{\pi}\int_0^{\theta_1}\int_0^{\infty} I_{bb}(T_a, \lambda)\varepsilon'(\lambda, \theta)\varepsilon_a(\lambda, \theta)cos(\theta)sin(\theta)d\lambda d\theta d\Phi$$

$$+ R_g\int_0^{\pi}\int_{\theta_3}^{\pi}\int_0^{\infty} I_{bb}(T_a, \lambda)\varepsilon'(\lambda, \theta)\varepsilon_a(\lambda, \theta)cos(\theta)sin(\theta)d\lambda d\theta d\Phi$$

Where P_{a_d} is the thermal radiative power absorbed from the ambient and directly emitted to the studied building wall, and P_{a_r} is the thermal radiative power absorbed from the ambient and reflected from the ground to the studied building wall. R_g is the spectral reflectivity of the ground. $\varepsilon_a(\lambda, \theta)$ is the emissivity of atmosphere, which can be given by $\varepsilon_a(\lambda, \theta) = 1 - t(\lambda)^{1/cos(\theta)}$, where t is the atmospheric transmission.

$$P_n(T_n) = P_{n\_d} + P_{n\_r}$$

$$= \int_0^{\pi}\int_{\theta_1}^{\theta_2}\int_0^{\infty} I_{bb}(T_n,\lambda)\varepsilon'(\lambda,\theta)\varepsilon_n(\lambda,\theta)cos(\theta)sin(\theta)d\lambda d\theta d\Phi$$

$$+ R_g \int_0^{\pi}\int_{\theta_2}^{\theta_3}\int_0^{\infty} I_{bb}(T_n,\lambda)\varepsilon'(\lambda,\theta)\varepsilon_n(\lambda,\theta)cos(\theta)sin(\theta)d\lambda d\theta d\Phi$$

Where P_{n_d} is the thermal radiative power absorbed from the neighboring object and directly emitted to the studied building wall, and P_{n_r} is the thermal radiative power absorbed from the neighboring object and reflected from the ground to the studied building wall. $\varepsilon_n(\lambda,\theta) = \varepsilon_{n,0}\, cos\left(\frac{\pi}{2} - \theta\right)$is the emissivity of neighboring object, and $\varepsilon_{n,0}$ is the assumed building surface emissivity.

$$P_g(T_g) = \int_0^{\pi}\int_{\theta_2}^{\pi}\int_0^{\infty} I_{bb}(T_g,\lambda)\varepsilon'(\lambda,\theta)\varepsilon_g(\lambda,\theta)cos(\theta)sin(\theta)d\lambda d\theta d\Phi$$

Where $\varepsilon_g(\lambda,\theta) = (1 - R_g)cos(\pi - \theta)$ is the emissivity of ground. As illustrated in Figure S8, θ_1, θ_2, and θ_3 are the boundary angles of the four different situations for the heat absorption to the studied building wall, and they can be calculated as: $\theta_1 = \tan^{-1}[D/(H_n - H_{wall})]$, $\theta_2 = \pi - \tan^{-1}(D/H_{wall})$, and $\theta_3 = \pi - \tan^{-1}[D/(H_{wall} + H_n)]$, respectively, where, D is the distance between the studied building wall and the neighboring object, H_n is the height of the neighboring object, and H_{wall} is the height of the calculated point on the studied building wall.

$$P_{conv}(T_{wall}, T_a) = h_c(T_{wall} - T_a)$$

Where h_c is the convective heat exchange coefficient.

Note S4. Outdoor field test

The outdoor field tests for examining the thermal regulation performance of our low-e paint were conducted on the rooftop of a three-story building at Purdue University, West Lafayette, IN, USA. In the field test, two structurally identical house models were constructed using the same 2 mm-thick wooden sheets with a thermal conductivity of 0.13 W m^{-1} K^{-1}, painted with black walls and a white roof. As shown in Supplementary Figure S13a, the house model can be depicted as a rectangular structure with dimensions of 15×15×10 cm and a triangular roof with a slope of 90°. Two K-type thermocouples were used for each house model to collect the wall temperature and the house air temperature. The thermocouple fixed at the center of the inner surface of the wall (15×15 cm surface) measured the wall temperature, referred to as "TC_wall". The thermocouple located in the center of the house model space measured the temperature of the inside air, referred to as "TC_air". One house termed the "commercial house", had its walls coated with commercial black paint, while the other, termed the "low-e house", had its walls coated with low-e black paint. The thermal emissivity for the commercial house wall and the low-e house wall were 0.95 and 0.31, respectively (Figure S13b). To minimize heat transfer effects from the roof and bottom of the houses and thereby highlight the thermal performance of the walls, the roofs were coated with ultra-white $BaSO_4$ paint with a solar reflectance of 97%[4]. Additionally, the bottoms of the houses were sealed with rigid insulating foam. The wall temperature and inside air temperature of the black house are "commercial wall" and "commercial air", respectively. Similarly, the wall temperature and inside air temperature of the low-e house are "low-e wall" and "low-e air", respectively. During the test, two houses were placed in parallel on a thick thermal insulation foam wrapped in Al foil, with the walls holding the thermocouples on the inner face facing eastward. The device was covered with a MIR-transparent film as a weather shield to reduce the convective heat loss without blocking the emitted radiation from the house walls. The ambient temperature was also measured by a K-type thermocouple near the device and covered with a plastic outer shield. The field tests were conducted from Dec. 13th to Dec. 14th, 2023, and Jan. 21st, 2024.

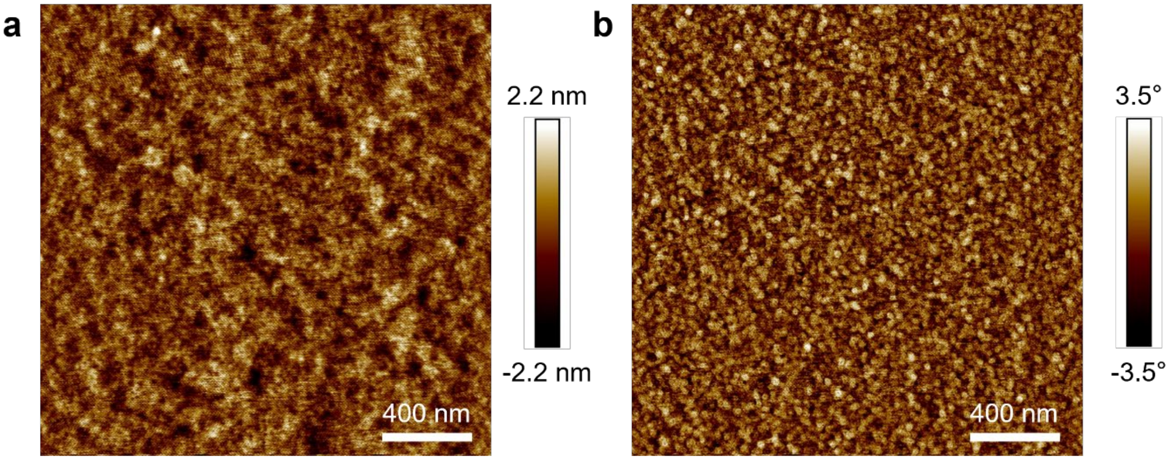

Figure S1. Atomic force microscopy a) height and b) phase images of spray-coated n-PBDF layer (*d* ~ 140 nm) on the commercial black paint layer.

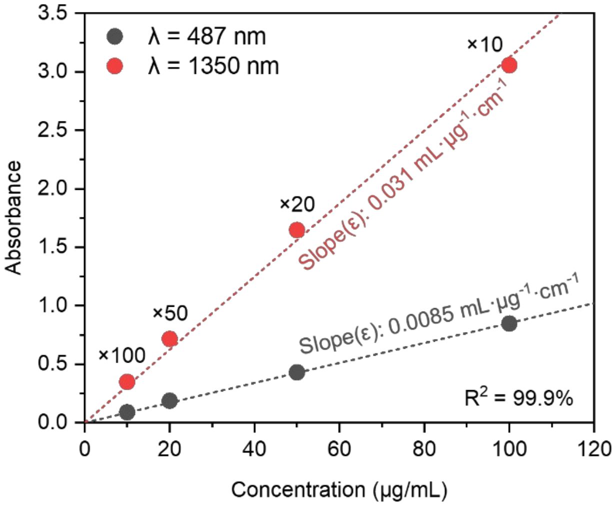

Figure S2. Beer-Lambert plot of absorbance at two different wavelengths (487 nm and 1350 nm in the visible and infrared range) versus the concentration of the low-e n-PBDF ink solution (light path length: 10 mm). The line is an unweighted proportional fit to the data with the slope of the extinction coefficient (unit: mL·μg^{-1}·cm^{-1}). The numbers above these points denote the scale factor of dilution.

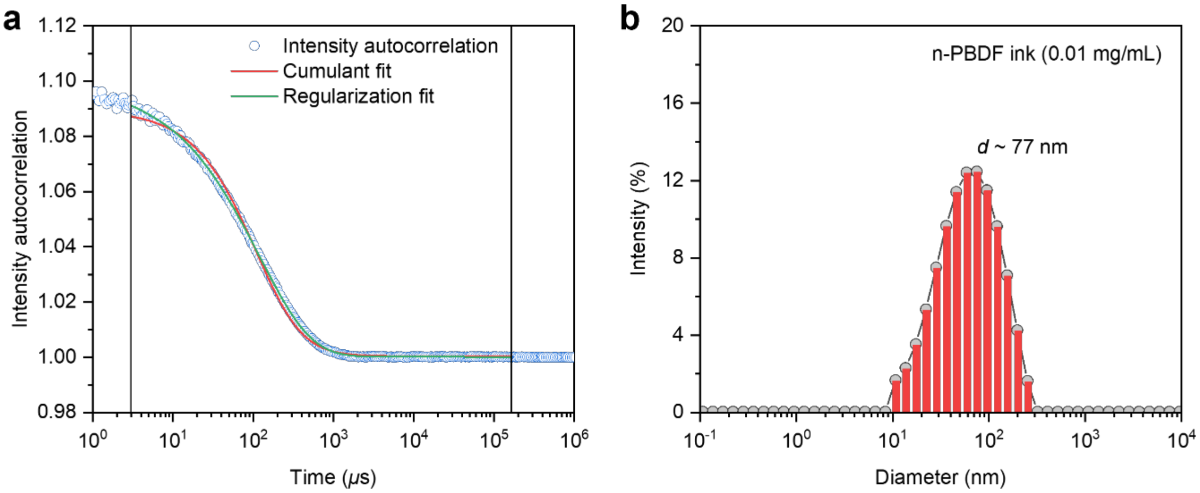

Figure S3. Physical features of n-PBDF-dispersed ink characterized using dynamic light scattering (DLS): a) the corresponding autocorrelation function (ACF), and b) DLS intensity profiles of hydrodynamic diameter distribution of n-PBDF inks through the Rayleigh sphere model.

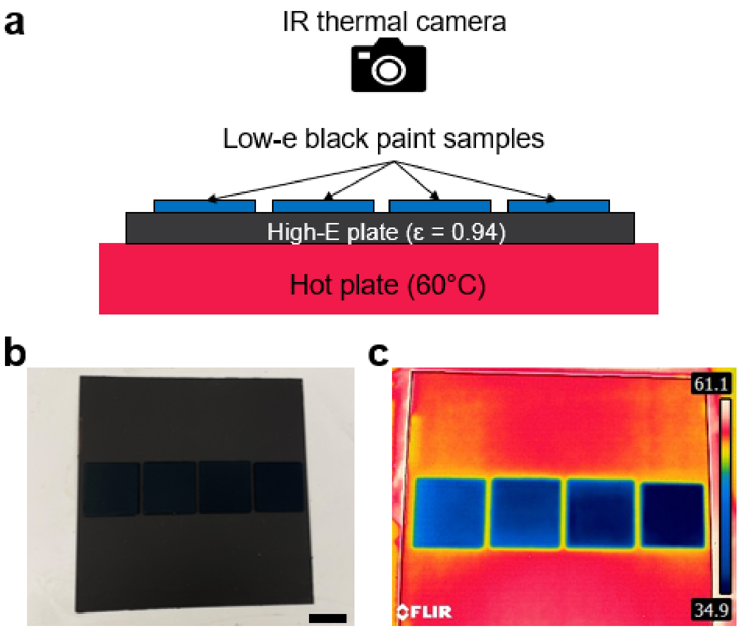

Figure S4. Visualized thermal effect of low-e black paints with different n-PBDF coating thicknesses. a) Schematic illustrating the experimental setup for taking the IR thermal images of low-e black paints using a thermal camera on a hot plate. The photo b) and the corresponding IR thermal image c) of low-e black paint samples. From left to right, the n-PBDF coating thicknesses for these four samples are 121 143, 168, and 194 nm, respectively. The scale bar in b) is 2 cm.

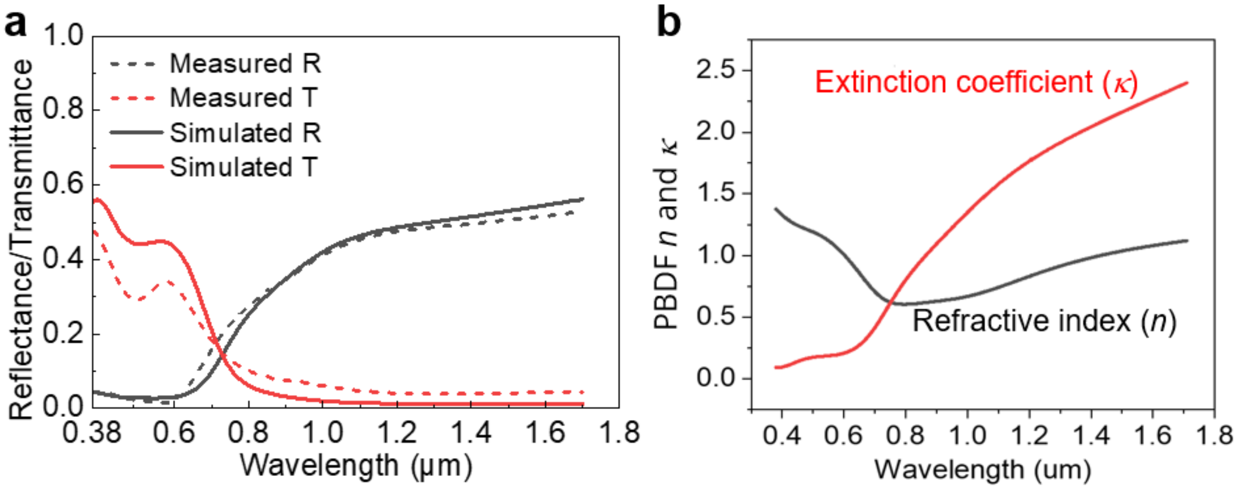

Figure S5. Spectra comparison for the n-PBDF coating layer. a) Measured and simulated spectra of a 168 nm thick n-PBDF particle coating layer coated on a 1 mm-thick glass slide. b) Refractive index and extinction coefficient of n-PBDF.

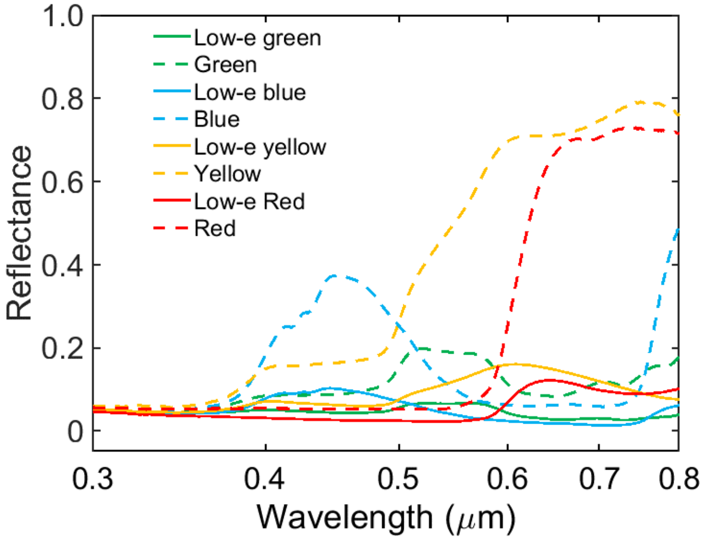

Figure S6. The reflectance spectra of commercial paints in green, blue, yellow, and blue and their corresponding low-e paints in the visible area from 0.3-0.8 μm.

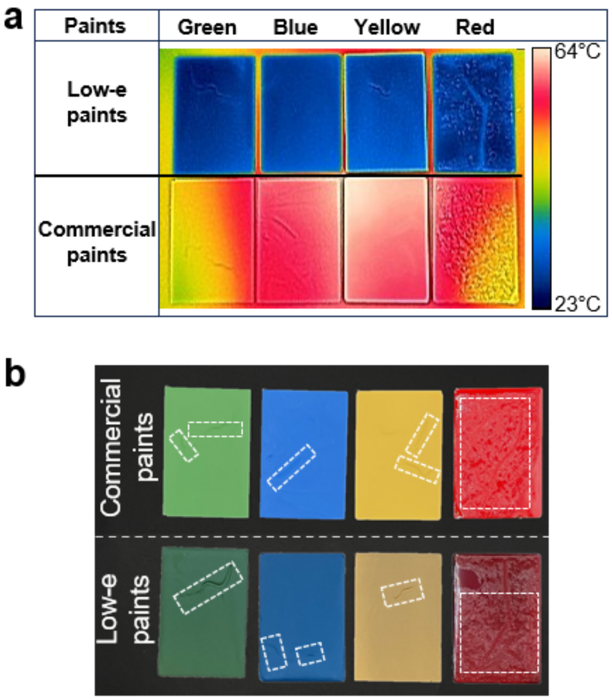

Figure S7. a) Infrared thermal image of colorful low-e paints (top row) and corresponding commercial paints (bottom row) in green, blue, yellow, and red (from left to right). b) Photographs showing the commercial-colored paints and the dual-layer low-e counterparts. The groove and wrinkle structures on both commercial paints and low-e paints are highlighted in dashed white rectangles. For both the infrared thermal images and photographs, the surface morphology of the samples is not entirely smooth, with grooves observed on the green, blue, and yellow paints (Sherwin-Williams) and a wrinkle-like structure present on the red paint (Rust-Oleum) samples. These features formed during the paint drying process. All paints were coated on 1 mm-thick glass slides in the dimension of 5×7.5 cm working as substrates. These samples were placed on a hot plate covered with a black metal plate, which has a surface emissivity of 0.94. The hot plate's temperature was set to 60°C. After the temperature stabilized, the IR thermal image was captured using the thermal camera at room temperature. Under the thermal camera, low-e paints have a very low surface temperature because their surface emissivity is very low, demonstrating restricted thermal radiation. In contrast, due to the high emissivity of commercial paints, their surface temperatures are much higher.

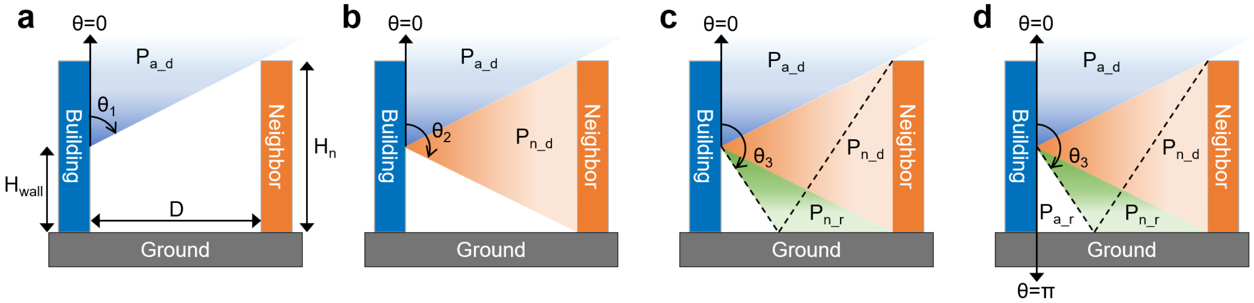

Figure S8. Radiative thermal absorption to the central point of the building wall with various zenith angles. a) $\theta = 0\ to\ \theta_1$: Thermal absorption from direct ambient emission; b) $\theta = \theta_1\ to\ \theta_2$: Thermal emission from direct neighboring object emission; c) $\theta = \theta_2\ to\ \theta_3$: Thermal absorption from reflected neighboring object emission; d) $\theta = \theta_3\ to\ \pi$: Thermal absorption from reflected ambient emission.

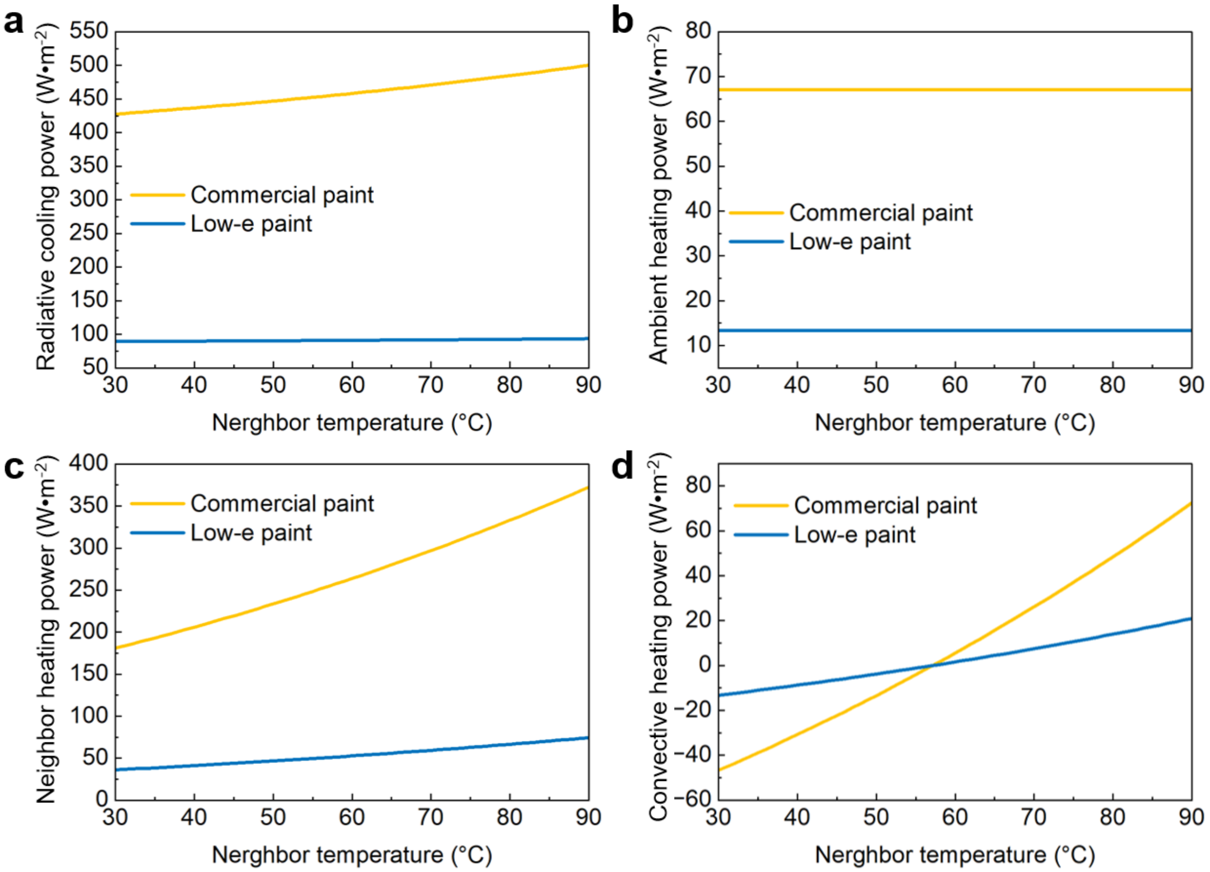

Figure S9. Simulated radiative power emitted to the outer space a), absorbed from ambient b), absorbed from neighboring objects c), and convective power exchanged with ambient d) for the studied building wall painted with commercial paint and low-e paint during hot climates.

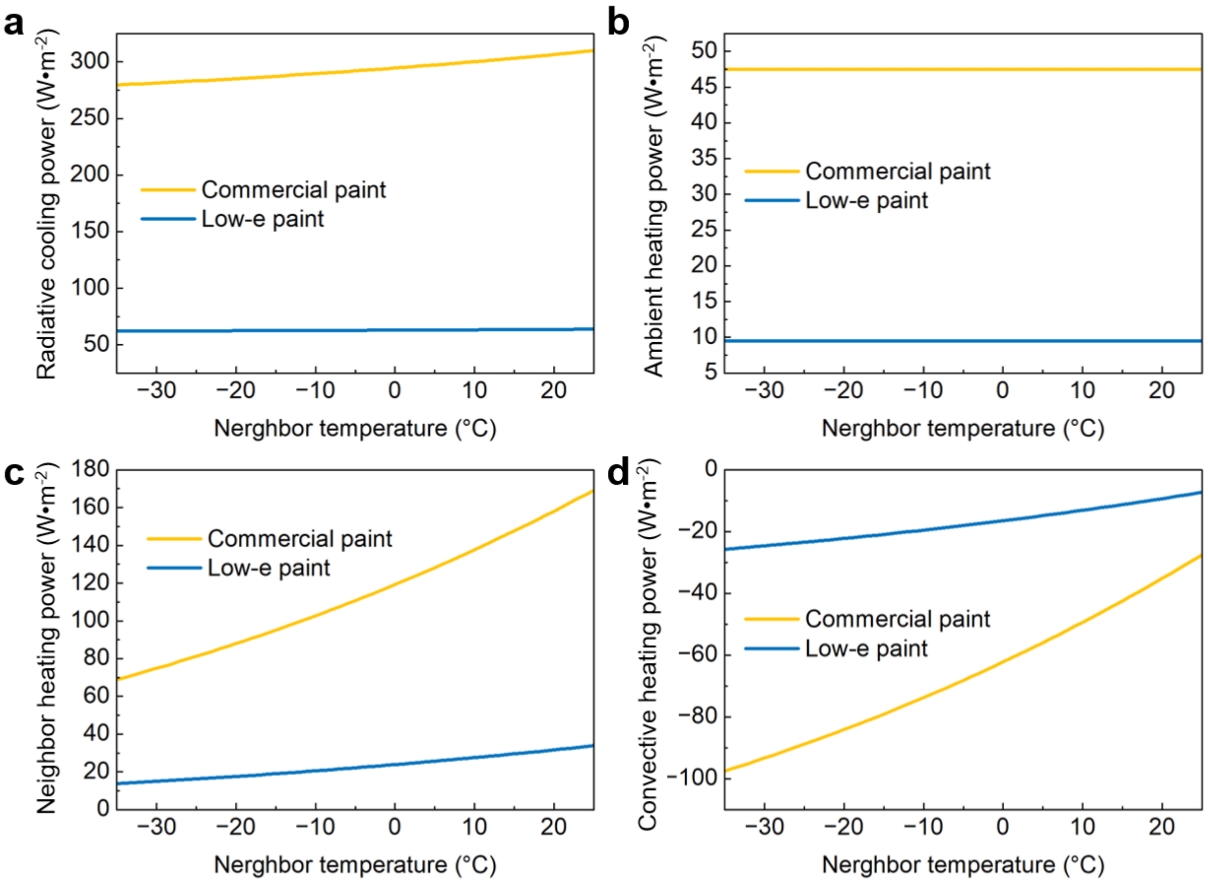

Figure S10. Simulated radiative power emitted to the outer space a), absorbed from ambient b), absorbed from neighboring object c), and convective power exchanged with ambient d) for the studied building wall painted with commercial paint and low-e paint during cold climate.

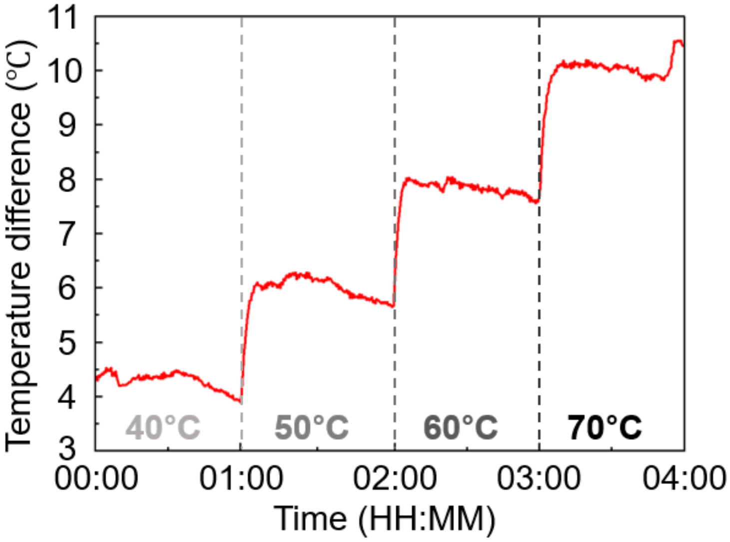

Figure S11. Temperature differences between commercial black paint and low-e black paint with the coating thickness of n-PBDF layer of 231 nm at various heating temperatures. The temperature values in the figure display the set temperature for the hot plates at each step with a time interval of 1 h.

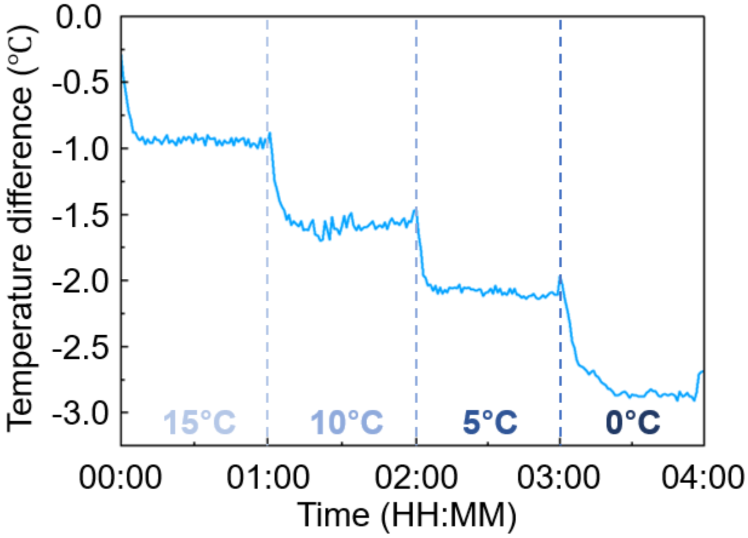

Figure S12. Temperature differences between commercial black paint and low-e black paint with the coating thickness of n-PBDF layer of 231 nm at various cooling temperatures. The temperature values in each figure display the set temperature for the cooling plates at each step with a time interval of 1 h.

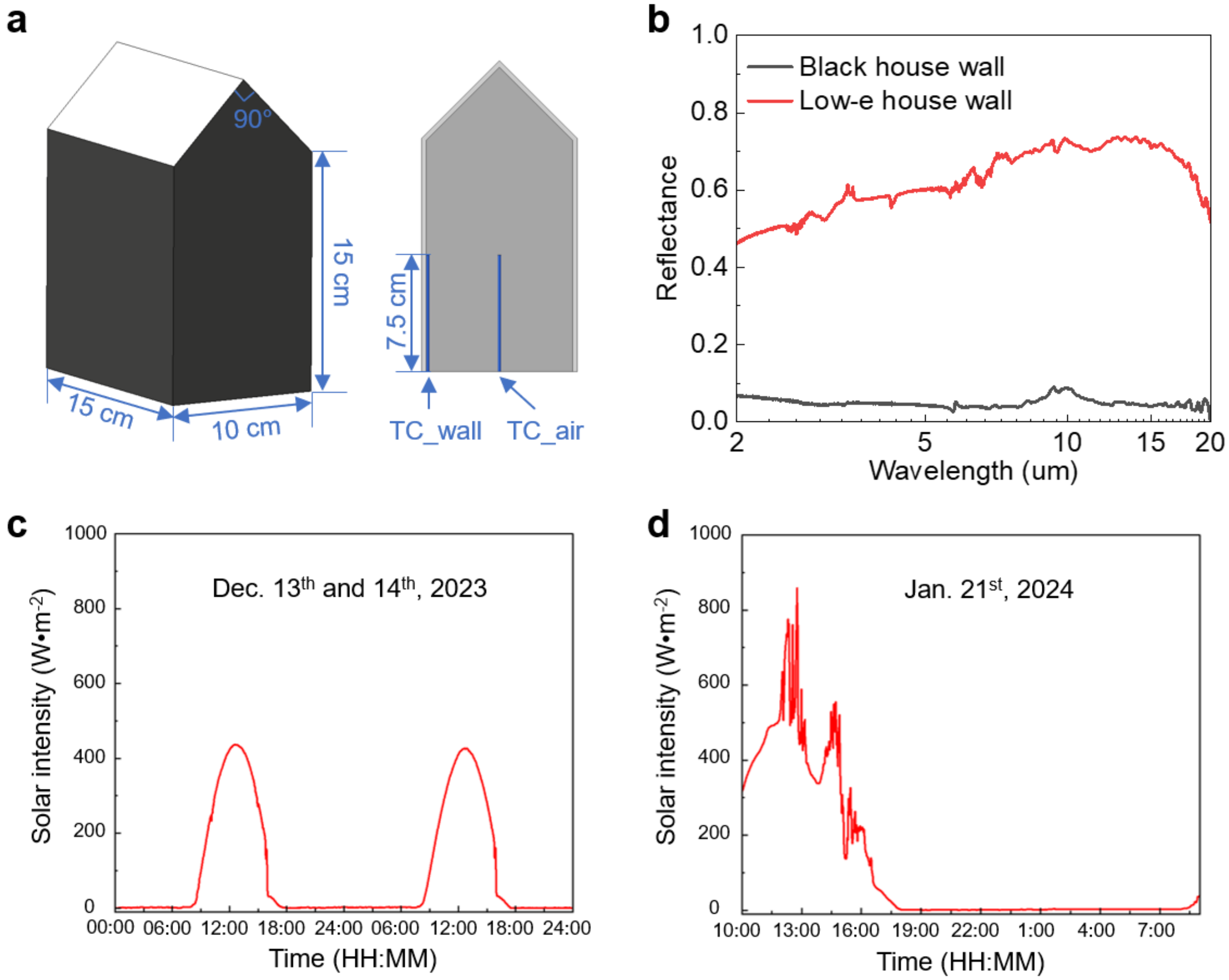

Figure S13. House model dimensions and ambient conditions for the field test. a) Schematically showing the dimensions of the hose used in the field test (left) and the fixed position of thermocouples in the house model (right). TC_wall is the thermocouple fixed at the center of the inner surface of the wall to measure the temperature of the wall. TC_air is the thermocouple fixed in the center of the house model space to measure the temperature of the inside air. b) Measured reflectance spectra of commercial black paint-coated wood board (black house wall) and low-e black paint-coated wood board (low-e house wall). Solar intensities for the field test on c) Dec. 13th and 14th, 2023, and on d) Jan. 21st, 2024.

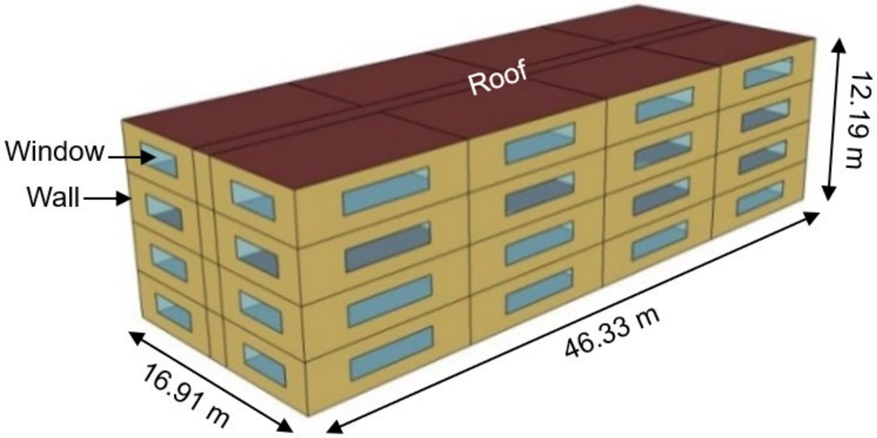

Figure S14. Midrise apartment model used in EnergyPlus for energy-saving evaluation of HVAC systems. For this apartment, the gross wall area is 7710.48 m^2 and the window opening area is 1146.45 m^2.

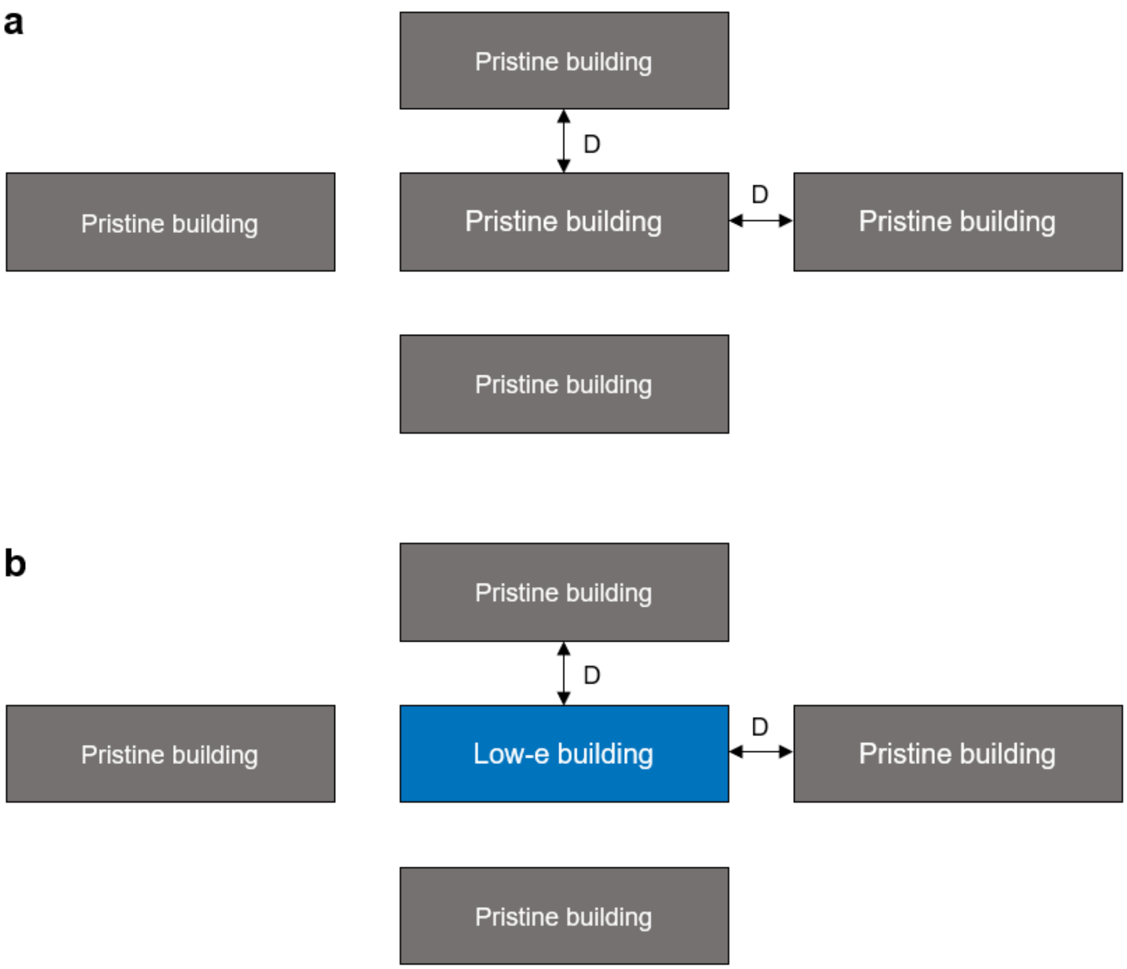

Figure S15. Schematic diagram of the building layout for the HVAC energy-saving simulation in EnergyPlus serving as a) baseline and b) experimental object. In the simulated model, the radiative energy from the surrounding buildings was considered. The studied building is surrounded by four buildings of the same size; that is, the four vertical walls of the studied building face a wall of the same size. All the surrounding buildings maintained the original parameters, aligned with conventional construction materials. a) shows the building layout for the baseline data in this simulation, where the central building is the original building. b) shows the layout of the experimental group data, where the central building is a low-e building with walls painted with low-e paint.

Table S1. Materials properties used in the energy-saving analysis of EnergyPlus

Materials	Thickness (m)	Thermal conductivity (W/ m K)	Density (kg/m^3)	Specific heat (J/kg K)	Thermal absorp.	Solar absorp.	Visible absorp.
Commercial black paint	0.0008	0.2	3174	1500	0.9	0.78	0.78
Low-e black paint	0.0008	0.2	3174	1500	0.9	0.78	0.78
Wood siding	0.01	0.11	545	1210	0.9	0.78	0.78
Steel frame resident wall insulation	0.07812	0.049	265	837	0.9	0.70	0.70
0.5-inch Gypsum board	0.0127	0.16	785	830	0.9	0.92	0.92

References

[1] Z. Ke, A. Abtahi, J. Hwang, K. Chen, J. Chaudhary, I. Song, K. Perera, L. You, K. N. Baustert, K. R. Graham, *J. Am. Chem. Soc.* **2023**, *145*, 3706.

[2] Y. Tian, X. Liu, Z. Wang, J. Li, Y. Mu, S. Zhou, F. Chen, M. L. Minus, G. Xiao, Y. Zheng, *Nano Energy* **2022**, *96*, 107085.

[3] M. Bae, D. H. Kim, S.-K. Kim, Y. M. Song, *Nanophotonics* **2024**.

[4] X. Li, J. Peoples, P. Yao, X. Ruan, *ACS Appl. Mater. Interfaces* **2021**, *13*, 21733.